# Phonon-induced dephasing in quantum-dot–cavity QED

A. Morreau* and E. A. Muljarov†
*School of Physics and Astronomy, Cardiff University, Cardiff CF24 3AA, United Kingdom*

(Received 27 July 2018; revised manuscript received 7 August 2019; published 24 September 2019)

We present a semianalytic and asymptotically exact solution to the problem of phonon-induced decoherence in a quantum dot-microcavity system. Particular emphasis is placed on the linear polarization and optical absorption, but the approach presented herein may be straightforwardly adapted to address any elements of the exciton-cavity density matrix. At its core, the approach combines Trotter's decomposition theorem with the linked cluster expansion. The effects of the exciton-cavity and exciton-phonon couplings are taken into account on equal footing, thereby providing access to regimes of comparable polaron and polariton timescales. We show that the optical decoherence is realized by real phonon-assisted transitions between different polariton states of the quantum-dot–cavity system, and that the polariton line broadening is well-described by Fermi's golden rule in the polariton frame. We also provide purely analytic approximations which accurately describe the system dynamics in the limit of longer polariton timescales.

DOI: 10.1103/PhysRevB.100.115309

## I. INTRODUCTION

A quantum dot (QD) embedded in a solid-state optical microcavity presents a fundamental system within cavity quantum electrodynamics (cavity-QED) [1]. The QD exciton couples to an optical mode of the cavity in a manner well described by the exactly solvable Jaynes-Cummings (JC) model [2–4]. Within the strong coupling regime, there is a partly reversible exchange of energy, with a period $\tau_{\rm JC}$, between the exciton and the cavity mode, which gives rise to *polariton* formation and characteristic vacuum Rabi splitting [5–7].

While not accounted for in the JC model, there is significant experimental and theoretical evidence [8–22] to suggest that phonons play a crucial role in the optical decoherence of the QD–cavity system. The general phenomenon of phonon-induced dephasing in semiconductor QDs is well studied; it has been successfully explained and quantified by the exactly solvable independent boson (IB) model [23]. This model describes a *polaron*, formed from a QD exciton coupled to bulk acoustic phonons [24], with a characteristic polaron formation time $\tau_{\rm IB}$. The IB model accounts for the major effect of the non-Markovian pure dephasing but is known to fail treating the exciton zero-phonon line (ZPL) broadening [25].

It is natural to draw upon the JC and IB models when addressing the problem of phonon-induced dephasing in the QD–cavity system. However, the combination of the two models presents a significant challenge. Various approaches to the QD–cavity problem have been suggested in the literature, ranging from Born-Markov approximations [8–10] to path-integral methods [14,15,26–31] and nonequilibrium Green's function techniques [17]. These approaches can be broadly divided into perturbative and nonperturbative methods.

The perturbative methods employ a polaron transformation followed by a perturbative treatment of the coupling of the phonon-dressed exciton to the cavity mode, carried out in the second-order Born approximation [8–11] or beyond [16,17]. These approaches perform well in certain parameter regimes but break down, for example, when the polaron formation time $\tau_{\rm IB}$ is comparable to, or slower than, the exciton-cavity oscillation period of the polariton $\tau_{\rm JC}$.

Nonperturbative techniques based on a quasiadiabatic Feynman path-integral scheme [26] enable accurate numerical solutions but are computationally expensive and provide little insight into the underlying physics. Nahri *et al.* [15] apply a tensor multiplication scheme [26] to the case of a QD–cavity system with superohmic spectral density. This technique relies upon a complex algorithm with an "on-the-fly path selection" optimization [27]. Glassl *et al.* [14] present a real-time path-integral scheme [28] adapted for a QD in a lossless cavity. Cavity and QD dampings are included within later work [29], but in this case the exciton-phonon coupling is added phenomenologically.

In this paper, we present a semianalytic exact solution of the long-standing problem of the phonon-induced decoherence of the QD–cavity system. Our approach is based on the Trotter decomposition with a subsequent use of the cumulant expansion technique [23,25,32], which provides a computationally straightforward and physically intuitive formulation. Being nonperturbative, our approach treats the effects of the exciton-photon and exciton-phonon couplings on equal footing, thereby rendering the technique appropriate across the full range of both coupling strengths, as well as timescales $\tau_{\rm IB}$ and $\tau_{\rm JC}$. We additionally provide a physical interpretation of our findings based on a theoretically rigorous polariton model.

## II. SYSTEM HAMILTONIAN AND TIMESCALES

A key principle of the present method is a separation of the system Hamiltonian into two exactly solvable parts,

*morreauai@cardiff.ac.uk
†Egor.Muljarov@astro.cf.ac.uk

 

$H = H_{\rm JC} + H_{\rm IB}$, described by the JC and IB models, respectively. The JC Hamiltonian has the form ($\hbar = 1$)

$$H_{\rm JC} = \omega_X d^\dagger d + \omega_C a^\dagger a + g(a^\dagger d + d^\dagger a), \tag{1}$$

where $d^\dagger$ ($a^\dagger$) is the exciton (cavity photon) creation operator, $g$ is the exciton-cavity coupling strength, and $\omega_X$ ($\omega_C$) is the exciton (cavity photon) complex frequency:

$$\omega_{X,C} = \Omega_{X,C} - i\gamma_{X,C}. \tag{2}$$

The imaginary frequency component $\gamma_X$ ($\gamma_C$) characterizes the long-time ZPL exciton dephasing (cavity mode radiative decay) rate. Note that this non-Hermitian Hamiltonian $H_{\rm JC}$ is straightforwardly derived from its Hermitian analog through the Lindblad dissipator formalism, as shown in Appendix A.

For convenience, the ZPL term from the standard IB Hamiltonian [23] has been included within $H_{\rm JC}$, Eq. (1), giving $H_{\rm IB}$ of the form

$$H_{\rm IB} = H_{\rm ph} + d^\dagger d V, \tag{3}$$

where $H_{\rm ph}$ is the free phonon bath Hamiltonian and $V$ describes the exciton-phonon interaction:

$$H_{\rm ph} = \sum_q \omega_q b_q^\dagger b_q, \quad V = \sum_q \lambda_q (b_q + b_{-q}^\dagger). \tag{4}$$

Here, $b_q^\dagger$ ($\omega_q$) is the creation operator (frequency) of the $q$th phonon mode and $\lambda_q$ is the matrix element of the exciton-phonon coupling.

It is instructive, at this point, to formally introduce timescales $\tau_{\rm JC}$ and $\tau_{\rm IB}$ associated with the JC and IB Hamiltonians, respectively. The polariton timescale $\tau_{\rm JC}$ characterizes the temporal period of the Rabi oscillations,

$$\tau_{\rm JC} = \frac{2\pi}{\Delta\omega}, \tag{5}$$

where $\Delta\omega$ is the polariton line separation. In the absence of phonons and for the case of zero detuning, $\Omega_X = \Omega_C$, the polariton Rabi splitting in the strong coupling regime is simply twice the exciton-cavity coupling strength: $\Delta\omega = 2g$.

We define the polaron timescale as

$$\tau_{\rm IB} \approx \sqrt{2}\pi l / v_s, \tag{6}$$

where $l$ is the exciton confinement radius and $v_s$ is the sound velocity, Throughout this paper, we take $l = 3.3$ nm and $v_s = 4.6 \times 10^3$ m/s. Note that Eq. (6) underestimates the polaron timescale at very low temperatures ($\lesssim$5 K)—see Appendix E for further discussion. Physically, the polaron timescale characterizes the time to form (disperse) a polaron cloud following creation (destruction) of an exciton.

## III. METHOD: TROTTER DECOMPOSITION WITH LINKED CLUSTER EXPANSION

While our approach is general and suited for describing the dynamics of any elements of the reduced density matrix of the JC subsystem, in this paper we concentrate on the most simple and intuitively clear quantity: the linear optical polarization. For this purpose, it is sufficient to reduce the basis of the JC system to the following three states: the absolute ground state $|0\rangle$, the excitonic excitation $|X\rangle$, and the cavity excitation $|C\rangle$. In this basis, $d^\dagger = |X\rangle\langle 0|$ and $a^\dagger = |C\rangle\langle 0|$. The linear polarization is then given by a $2\times 2$ matrix $\hat{P}(t)$ with the matrix elements $P_{jk}(t)$ expressed in terms of the time-evolution operator $\hat{U}(t)$ as

$$P_{jk}(t) = \langle\langle j|\hat{U}(t)|k\rangle\rangle_{\rm ph}, \quad \hat{U}(t) = e^{iH_{\rm ph}t} e^{-iHt}, \tag{7}$$

where $\langle\ldots\rangle_{\rm ph}$ denotes the expectation value over all phonon degrees of freedom in thermal equilibrium and $j, k = X, C$, see Appendix A for details. Here, $j$ indicates the initial excitation mode of the system and $k$ the mode in which the polarization is measured. For example, $P_{XX}$ ($P_{CC}$) denotes the excitonic (photonic) polarization under a pulsed exciton (cavity) excitation.

Using Trotter's decomposition theorem, the time-evolution operator $\hat{U}(t)$ can be re-expressed as

$$\hat{U}(t) = \lim_{\Delta t\to 0} e^{iH_{\rm ph}t}(e^{-iH_{\rm IB}\Delta t} e^{-iH_{\rm JC}\Delta t})^N, \tag{8}$$

where $\Delta t = t/N$. We introduce two new operators, $\hat{M}$ and $\hat{W}$, associated with the JC and IB Hamiltonians, respectively,

$$\hat{M}(t_n - t_{n-1}) = \hat{M}(\Delta t) = e^{-iH_{\rm JC}\Delta t}, \tag{9}$$

$$\hat{W}(t_n, t_{n-1}) = e^{iH_{\rm ph}t_n} e^{-iH_{\rm IB}\Delta t} e^{-iH_{\rm ph}t_{n-1}}, \tag{10}$$

where $t_n = n\Delta t$. Exploiting the commutivity of $H_{\rm JC}$ and $H_{\rm ph}$ enables us to express the time-evolution operator as a time-ordered product of pairs $\hat{W}\hat{M}$:

$$\hat{U}(t) = \mathcal{T}\prod_{n=1}^{N} \hat{W}(t_n, t_{n-1})\hat{M}(t_n - t_{n-1}), \tag{11}$$

where $\mathcal{T}$ is the time ordering operator. Noting that both $\hat{W}$ and $\hat{M}$ are $2\times 2$ matrices in the $|X\rangle$, $|C\rangle$ basis and that $\hat{W}$ is diagonal (with diagonal elements $W_i$), the polarization Eq. (7) takes the form

$$P_{jk}(t) = \sum_{i_{N-1}=X,C} \cdots \sum_{i_1=X,C} M_{i_N i_{N-1}} \cdots M_{i_2 i_1} M_{i_1 i_0} \times \langle W_{i_N}(t, t_{N-1}) \cdots W_{i_2}(t_2, t_1) W_{i_1}(t_1, 0)\rangle_{\rm ph}, \tag{12}$$

where $i_N = j$, $i_0 = k$, $M_{i_n i_m} = [\hat{M}(\Delta t)]_{i_n i_m}$, and

$$W_{i_n}(t_n, t_{n-1}) = \mathcal{T}\exp\left\{-i\delta_{i_n X}\int_{t_{n-1}}^{t_n} V(\tau)d\tau\right\}, \tag{13}$$

with $\delta_{ij}$ the Kronecker delta and $V(\tau) = e^{iH_{\rm ph}\tau} V e^{-iH_{\rm ph}\tau}$. Further details and intermediate steps are provided in Appendix B.

It is instructive at this point to introduce the concept of a "realization" of the system as a particular combination of indices $i_n$ within the full summation of Eq. (12). We associate with each realization a step function $\hat{\theta}(\tau)$ being equal to 0 over the time interval $t_n - t_{n-1}$ if $i_n = C$ (the system is in the cavity state $|C\rangle$) or 1 if $i_n = X$ (the system is in the excitonic state $|X\rangle$). An example realization is given in Appendix C. The product of $W$ operators for a particular realization can be written as

$$W_{i_N}(t, t_{N-1}) \cdots W_{i_1}(t_1, 0) = \mathcal{T}\exp\left\{-i\int_0^t \bar{V}(\tau)d\tau\right\}, \tag{14}$$

where $\bar{V}(\tau) = \hat{\theta}(\tau)V(\tau)$. Now, applying the linked cluster theorem [23] for calculating the trace of Eq. (14) over all

phonon states, we obtain

$$\langle W_{i_N}(t,t_{N-1})\cdots W_{i_2}(t_2,t_1)W_{i_1}(t_1,0)\rangle_{\rm ph} = e^{\bar{K}(t)}, \tag{15}$$

where

$$\bar{K}(t) = -\frac{1}{2}\int_0^t d\tau_1 \int_0^t d\tau_2 \langle \mathcal{T}\bar{V}(\tau_1)\bar{V}(\tau_2)\rangle \tag{16}$$

is the linear cumulant for the particular realization. Its explicit dependence on the specific indices $i_n$ of the realization is given by

$$\bar{K}(t) = \sum_{n=1}^{N}\sum_{m=1}^{N}\delta_{i_nX}\delta_{i_mX}K_{|n-m|}, \tag{17}$$

where

$$K_{|n-m|} = -\frac{1}{2}\int_{t_{n-1}}^{t_n} d\tau_1 \int_{t_{m-1}}^{t_m} d\tau_2 \langle \mathcal{T}V(\tau_1)V(\tau_2)\rangle. \tag{18}$$

Note that $K_{|n-m|}$ depends only on the time difference $|t_n - t_m| = \Delta t|n-m|$. Furthermore, as shown in Appendix D, all $K_{|n-m|}$ can be efficiently calculated from the standard IB model cumulant $K(t) = \mathcal{T}\exp\{-i\int_0^t V(\tau)d\tau\}$ (calculation of the latter is detailed in Appendices E and F).

Keeping in mind an application of this theory to semiconductor QDs coupled to bulk acoustic phonons, we use the conditions of the superohmic coupling spectral density and a finite phonon memory time [28]. This permits a dramatic reduction in the number of terms within the double summation of Eq. (17). Indeed, we need to take into account only instances in which $|t_m - t_n| \leqslant \tau_{\rm IB}$. When selecting $\Delta t$, we must also be mindful of the requirement imposed by the Trotter decomposition method: $\Delta t \to 0$. In practice, $\Delta t$ must simply be small relative to the period of oscillation between exciton and cavity states $\tau_{\rm JC}$.

### A. Nearest Neighbors

We initially consider the most straightforward application of the technique, which will be referred to as the nearest-neighbors (NN) approach.

In the NN approach, we limit our consideration to $|n-m|\leqslant 1$, selecting $\Delta t \approx \tau_{\rm IB}$ so as to best satisfy both aforementioned conditions on $\Delta t$. The summation over $n$ and $m$ in Eq. (17) is therefore simplified to

$$\bar{K}(t) = \delta_{i_NX}K_0 + \sum_{n=1}^{N-1}\delta_{i_nX}(K_0 + 2\delta_{i_{n+1}X}K_1). \tag{19}$$

Crucially, as shown in Appendix C, this reduction to a single summation allows us to re-express Eq. (12) as

$$P_{jk}(t) = e^{\delta_{jX}K_0}\sum_{i_{N-1}}\cdots\sum_{i_1} G_{i_Ni_{N-1}}\cdots G_{i_2i_1}M_{i_1k}, \tag{20}$$

where

$$G_{i_ni_{n-1}} = M_{i_ni_{n-1}}e^{\delta_{i_{n-1}X}(K_0+2\delta_{i_nX}K_1)}. \tag{21}$$

Equation (20) can be compactly written in $2\times 2$ matrix form in the $|X\rangle$, $|C\rangle$ basis,

$$\hat{P}(t) = \begin{pmatrix} P_{XX} & P_{XC} \\ P_{CX} & P_{CC}\end{pmatrix} = \begin{pmatrix} e^{K_0} & 0 \\ 0 & 1\end{pmatrix}\hat{G}^{N-1}\hat{M}, \tag{22}$$

with $\hat{G}$ given by

$$\hat{G} = \begin{pmatrix} M_{XX}e^{K_0+2K_1} & M_{XC} \\ M_{CX}e^{K_0} & M_{CC}\end{pmatrix}. \tag{23}$$

As discussed in Sec. IV, the polarization matrix element $P_{XX}(t)$ comprises an initial rapid decay (on the scale of $\lesssim$10 ps) alongside long-time asymptotics. Our time step $\Delta t \approx \tau_{\rm IB}$ is too large to capture the former [24,25]. There is, however, a simple solution to this problem: For all $t < \tau_{\rm IB}$, we replace our fixed $\Delta t$ with a variable $\Delta t' = t/2$. This ensures that $\bar{K}$ is calculated exactly for all $t < \tau_{\rm IB}$. Further details on this modification are provided in Appendix D.

### B. Analytic long-time asymptotics

From the NN result Eq. (22), one can extract a simple analytic expression that describes the long-time behavior of the linear optical response. We use the asymptotic behavior of the standard IB model cumulant $K(t)$ in the long-time regime [24,25],

$$K(t) \approx -i\Omega_p t - S, \tag{24}$$

where $\Omega_p$ is the polaron shift and $S$ is the Huang-Rhys factor (the explicit forms of which are provided in Appendix E). This allows us to make the approximations $K_0 \approx -i\Omega_p\Delta t - S$ and $K_1 \approx S/2$. In the limit $\Delta t \approx \tau_{\rm IB} \ll \tau_{\rm JC}$, this results in a fully analytic long-time dependence of the polarization (see Appendix G for further details),

$$\hat{P}(t) \approx e^{-\hat{S}/2}e^{-i\tilde{H}t}e^{-\hat{S}/2} \quad (t > \tau_{\rm IB}), \tag{25}$$

where

$$\tilde{H} = \begin{pmatrix} \omega_X + \Omega_p & ge^{-S/2} \\ ge^{-S/2} & \omega_C\end{pmatrix}, \quad \hat{S} = \begin{pmatrix} S & 0 \\ 0 & 0\end{pmatrix}. \tag{26}$$

Comparing the long-time analytics for $P_{jk}(t)$, given by Eqs. (25) and (26), with the exact linear polarization in the JC model (no phonons), $\langle j|e^{-iH_{\rm JC}t}|k\rangle$, we see that the effect of acoustic phonons in this limit ($\tau_{\rm IB} \ll \tau_{\rm JC}$) is a reduction of the exciton-cavity coupling strength $g$ by a factor of $e^{S/2}$ and the ZPL weight of the excitonic polarization by a factor of $e^S$. Additionally, the bare exciton frequency is polaron shifted: $\omega_X \to \omega_X + \Omega_p$. These facts are consistent with the analytic results of the IB model and are in agreement with previous experimental and theoretical works [8,33]. Furthermore, we note that the form of the modified Hamiltonian $\tilde{H}$ given by Eq. (26) is exactly the same as obtained after making the polaron transformation of the full Hamiltonian $H$. This result therefore provides a rigorous proof of the fact that the polaron-transformed Hamiltonian $\tilde{H}$ can indeed be used as the unperturbed system, as it is done in the polaron master-equation approaches [8,16].

### C. *L*-Neighbors

We now address a general case in which the polaron and polariton timescales can be comparable, $\tau_{\rm IB} \sim \tau_{\rm JC}$, for example, in the case of a much larger exciton-cavity coupling $g$. This implies that we must find a way to reduce the time-step $\Delta t$ in the Trotter decomposition. We achieve this by going beyond the NN regime to the $L$-neighbor ($L$N) regime, where $L$ indicates the number of neighbors that we consider,

corresponding to the condition $|n-m| \leqslant L$ in Eq. (17). The aforementioned condition $\Delta t \ll \tau_{\rm JC}$ applies equally to the $L$N regime, and therefore in this regime we are bound by the constraint $L\Delta t \gtrsim \tau_{\rm IB}$. Importantly, this allows us to treat comparable polaron and polariton timescales provided that we choose $L$ such that the condition $\tau_{\rm IB}/L \ll \tau_{\rm JC}$ is satisfied.

In the $L$N approach, we define a quantity $F^{(n)}_{i_L\cdots i_1}$ which is generated via a recursive relation,

$$F^{(n+1)}_{i_L\cdots i_1} = \sum_{l=X,C} G_{i_L\cdots i_1 l} F^{(n)}_{i_{L-1}\cdots i_1 l}, \tag{27}$$

using $F^{(1)}_{i_L\cdots i_1} = M_{i_1 k}$ as the initial value, where $\hat{M}$ is defined as before by Eq. (9), while $G_{i_L\cdots i_1 l}$ is the $L$N analog of Eq. (21):

$$G_{i_L\cdots i_1 l} = M_{i_1 l} e^{\delta_{lX}(K_0 + 2\delta_{i_1 X}K_1 \cdots + 2\delta_{i_L X}K_L)}. \tag{28}$$

The polarization is then given by

$$P_{jk}(t) = e^{\delta_{jX}K_0} F^{(N)}_{C\cdots C j}. \tag{29}$$

Equations (27)–(29) present an asymptotically exact solution for the linear polarization. By extending the matrix size of the operators involved, it is straightforward to generalize this result to other correlators, such as the photon indistinguishability [17,34,35] or to other elements of the density matrix, such as the four-wave mixing polarization [4,36].

## IV. RESULTS

### A. Polarization and absorption spectra

To directly compare the various implementations of the Trotter decomposition method, we now apply the above-described formalisms to a system with realistic QD parameters [4,36] in the regime of relatively small QD–cavity coupling ($g = 50\,\mu$eV). Figure 1(a) shows the linear excitonic polarization $|P_{XX}(t)|$ calculated according to the analytic and NN techniques, Eqs. (25) and (22), respectively. Also shown is the "exact" polarization, calculated according the $L$-neighbor implementation, Eq. (29), with $L = 15$. In principle, one must take the limit $L \to \infty$ for a truly "exact" solution. For practical purposes, however, we select finite $L$ based on the desired accuracy; the 15-neighbor implementation provides a relative error in polarization of less than 0.1% for the present set of parameters.

Figure 1(b) shows the excitonic absorption spectra for $g = 50\,\mu$eV and zero detuning, calculated according to the above-described techniques. The absorption may be easily extracted from the linear polarization by taking the real part of the Fourier transform of $P_{XX}(t)$. The long-time behavior of the polarization is biexponential, as is clear from Eq. (25). The absorption spectrum therefore consists of a well-resolved polariton doublet, described by the eigenvalues $\omega_j = \Omega_j - i\Gamma_j$ ($j = 1, 2$) of the effective Hamiltonian Eq. (26). Although not accounted for within the analytic model, there is a rapid initial decay in the polarization $|P_{XX}(t)|$; this short-time behavior correlates to the phonon broadband (BB) within the absorption spectrum. At lower temperatures, the BB is more asymmetric and the ZPL weight is increased, in agreement with the IB model. For the parameters selected and $T = 50$ K, we find $\tau_{\rm IB} \approx 3.2$ ps and $\tau_{\rm JC} \approx \pi e^{S/2}/g \approx 57$ ps [see Eqs. (5) and (6) alongside Appendices E and F], so the NN approach presents a good approximation in this regime. As expected,

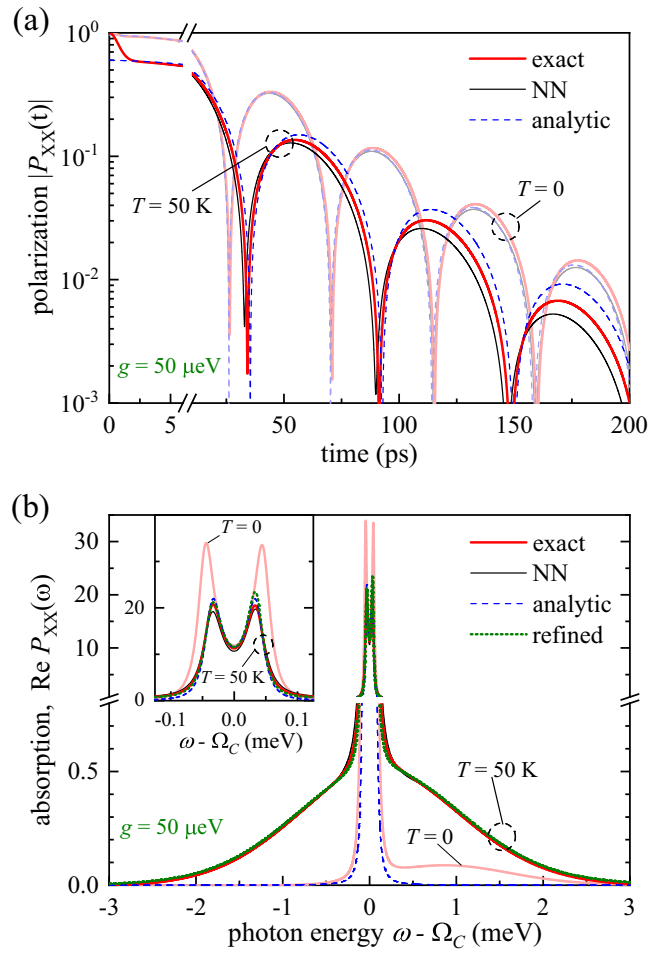


FIG. 1. (a) Excitonic linear polarization and (b) absorption for $T = 0$ and 50 K, calculated in the $L$N approach with $L = 15$ (red thick solid lines), NN approach with $L = 1$ (black thin solid lines), analytic approximation Eq. (25) (blue dashed lines), and refined analytics Eq. (H26) (green dotted line). We use the realistic parameters of InGaAs QDs studied in Refs. [25,32] and micropillars studied in Refs. [4,36] (also see Appendix F for details), including $g = 50\,\mu$eV, $\omega_X = \Omega_X - i\gamma_X$ with $\Omega_X = 1329.6$ meV and $\gamma_X = 2\,\mu$eV; $\omega_C = \Omega_C - i\gamma_C$ with $\Omega_C = \Omega_X + \Omega_p$, $\Omega_p = -49.8\,\mu$eV and $\gamma_C = 30\,\mu$eV. Inset: Linear plot of the absorption with limited frequency range.

the analytic result Eq. (25) describes the long-time dynamics well but fails at short times, as it is clear from Fig. 1(a). This is manifested in the absorption spectrum in Fig. 1(b) as an absence of the BB. To improve on this shortcoming, we have additionally developed a *refined*, fully analytic solution (distinct from the above-described Trotter decomposition method) which captures the BB and reproduces the whole spectrum to very good accuracy in this regime; see the green dotted line in Fig. 1(b) and Appendix H for details of the model. Appendix H also provides a calculation for a nonzero detuning, see Figs. 10 and 11.

In regimes of comparable polaron and polariton times $\tau_{\rm IB} \sim \tau_{\rm JC}$ (achieved by increasing the QD–cavity coupling constant to $g = 0.6$ meV while fixing all other parameters), the NN approach and the analytic approximations fail, leaving only the $L$N results. From the latter, we find that the long-time

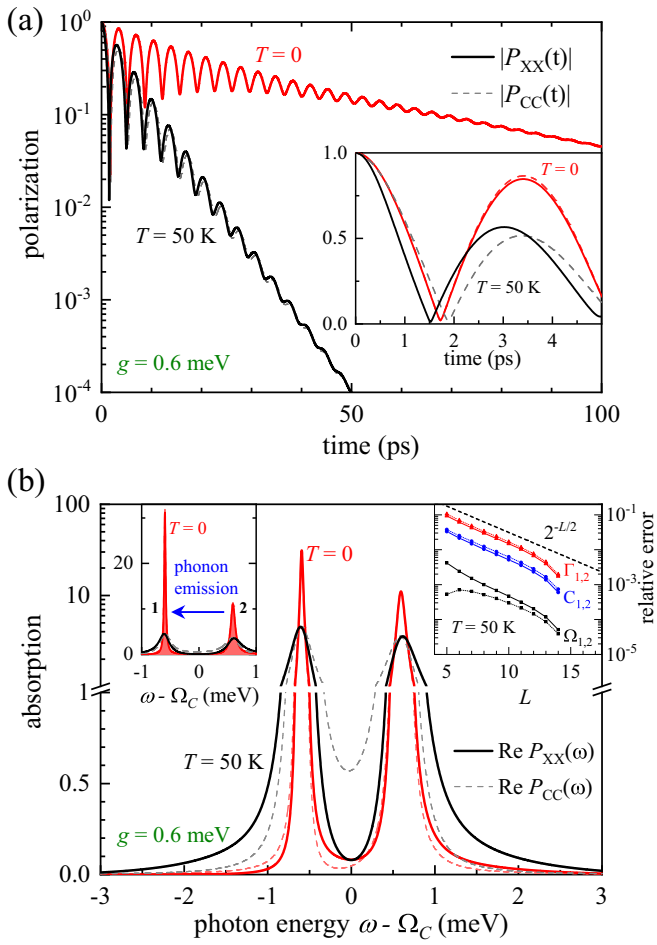


FIG. 2. As Fig. 1 but for $g = 0.6$ meV and only $L$N result shown, for $T = 0$ (red lines) and 50 K (black lines). The photon polarization and absorption are also shown (dashed lines). Insets: (a) the initial polarization dynamics; (b), left, linear plot of the absorption illustrating the $2 \to 1$ polariton transition assisted by phonon emission; (b), right, the relative error for the parameters of the long-time bi-exponential dependence of $P_{XX}(t)$, Eq. (30), as a function of the number of neighbors $L$, taking $L = 15$ as the exact solution.

dynamics of the polarization matrix remains biexponential,

$$\hat{P}(t) \approx \sum_{j=1}^{2} \hat{C}_j e^{-i\Omega_j t - \Gamma_j t} \quad (t > \tau_{\rm IB}), \tag{30}$$

where $\Omega_j$ ($\Gamma_j$) are the polariton frequencies (linewidths) and $\hat{C}_j$ are the amplitude matrices.

The linear excitonic and cavity polarizations, $|P_{XX}(t)|$ and $|P_{CC}(t)|$, are shown in Fig. 2(a). There is a pronounced damping of the beating of the two exponentials, even for zero detuning (shown). This implies that the two peaks within the absorption spectra now have quite different linewidths, as is clear from Fig. 2(b).

The observed behavior can be understood in terms of real phonon-assisted transitions between the states of the polariton doublet [22,37]. The variation in linewidths between $T = 0$ K and $T = 50$ K shown in Fig. 2(b) is clear evidence of the phonon-induced broadening mechanism. At $T = 0$, the

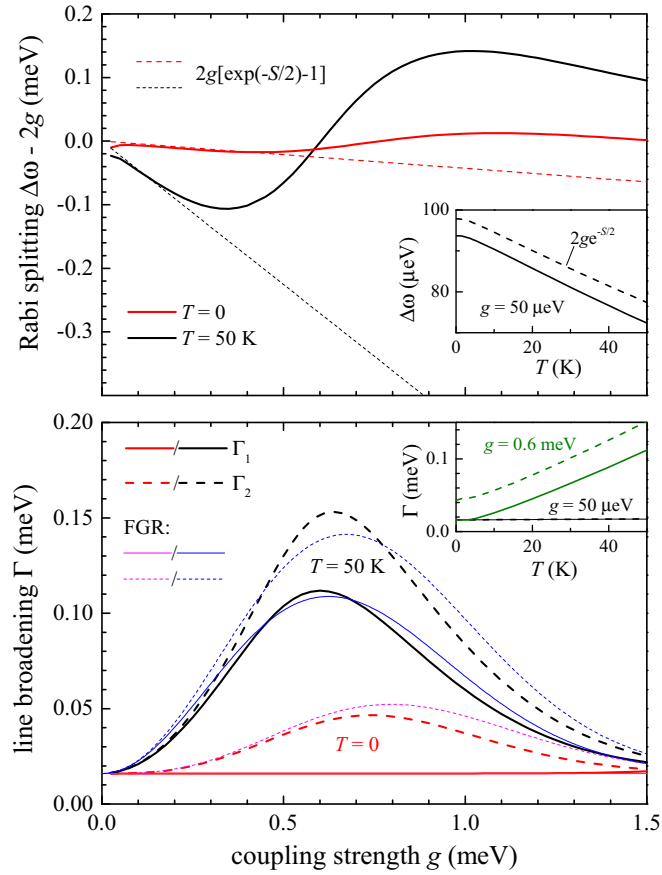


FIG. 3. Upper panel: Deviation of the polariton Rabi splitting $\Delta\omega = \Omega_2 - \Omega_1$, calculated via the $L$N model with $L = 15$, from the nominal Rabi splitting $2g$ (solid lines), as a function of the exciton-cavity coupling strength $g$ for zero effective detuning, $\omega_C = \omega_X + \Omega_p$, and two different temperatures, $T = 0$ and $T = 50$ K. The deviation of the phonon renormalized Rabi splitting from the nominal Rabi splitting $2g(e^{-S/2} - 1)$ is shown by dashed lines. Inset in upper panel: The calculated full Rabi splitting $\Delta\omega$ (solid line) for $g = 50\,\mu$eV as a function of the temperature $T$, in comparison with $2ge^{-S/2}$ (dashed lines). Lower panel: Linewidths $\Gamma_{1,2}$ of the lower (solid lines) and upper (dashed lines) polariton states in Eq. (30) as functions of the coupling strength $g$, calculated in the $L$N approach with $L = 15$ (thick black and red lines) and estimated according to Fermi's golden rule (thin blue and magenta lines). Inset in lower panel: Temperature dependence of $\Gamma_{1,2}$ for $g = 50\,\mu$eV (black) and 0.6 meV (green).

high-energy polariton state (2) is significantly broader than the low-energy state (1) due to the allowed transition $2 \to 1$, accompanied by emission of an acoustic phonon, as illustrated in the left inset of Fig. 2(b). At elevated temperatures both transitions $2 \to 1$ and $1 \to 2$, with phonon emission and absorption, respectively, are allowed, giving rise to more balanced linewidths. The line broadening as a function of temperature $T$ is shown in the inset of Fig. 3.

### B. Polariton line parameters

Increasing the exciton-cavity coupling strength $g$ beyond 0.6 meV (up to 1.5 meV), we find that the asymptotic behavior of the polarization retains the biexponential form of Eq. (30),

thereby enabling direct comparison of polariton parameters at various coupling strengths $g$. The polariton line splitting $\Delta\omega = \Omega_2 - \Omega_1$ and linewidths $\Gamma_{1,2}$ are shown against $g$ in Fig. 3, while the behavior of the amplitude matrices $\hat{C}_{1,2}$ with $g$ is addressed in Appendix I, see Fig. 12.

The upper panel of Fig. 3 shows the Rabi splitting $\Delta\omega$ of the polariton lines as a function of $g$, up to $g = 1.5$ meV. In the regime of small $g$, the analytic calculation of Eqs. (25) and (26) predicts a phonon-renormalized Rabi splitting of $\Delta\omega = 2ge^{-S/2}$ where $S$ is the Huang-Rhys factor defined in Appendix E. This dependence is indeed observed in the 15-neighbor calculation for coupling strength $g$ below 0.2 meV (0.5 meV) for $T = 50$ K ($T = 0$). A minor deviation from the analytic formula prediction of $\Delta\omega = 2ge^{-S/2}$ at small $g$ is due to finite exciton and cavity lifetimes used in the calculation: $\gamma_X = 2\,\mu$eV and $\gamma_C = 30\,\mu$eV. At larger $g$, the analytic prediction breaks down, and the Rabi splitting may even be enhanced by the presence of phonons.

## V. PHYSICAL INTERPRETATION: THE POLARITON PICTURE

The broadening $\Gamma_{1,2}$ of the polariton lines is strongly dependent on the exciton-cavity coupling strength $g$, as shown in the lower panel of Fig. 3. Maximal broadening occurs when the polariton splitting $\Delta\omega = \Omega_2 - \Omega_1$ corresponds to the typical energy of local acoustic phonons [32] (0.5 – 1 meV for the QDs under consideration). To understand and quantify this behavior, we make a unitary transformation of the Hamiltonian $H = H_{\rm JC} + H_{\rm IB}$,

$$H \to H' = \hat{Y} H \hat{Y}^{-1}, \tag{31}$$

where $\hat{Y}$ is the $2 \times 2$ matrix that diagonalizes the JC Hamiltonian $H_{\rm JC}$, comprising diagonal elements $\alpha$ and off-diagonal elements $\pm\beta$ (see Appendix G for explicit forms of $\hat{Y}$, $\alpha$, and $\beta$). In making this transformation, we move from an exciton-cavity basis ($d^\dagger$, $a^\dagger$) to a polariton basis ($p^\dagger_{1,2}$). The transformed Hamiltonian $H'$ has the form

$$H' = \begin{pmatrix} \omega_1 + \alpha^2 V & \alpha\beta V \\ \alpha\beta V & \omega_2 + \beta^2 V \end{pmatrix} + H_{\rm ph}\mathbb{1}, \tag{32}$$

where $\omega_{1,2}$ are the eigenvalues of the JC Hamiltonian $H_{\rm JC}$ (see Appendix G for explicit forms), $V$ and $H_{\rm ph}$ are defined in Eq. (4), and $\mathbb{1}$ is a $2 \times 2$ identity matrix in the polariton basis.

From Eq. (32), it is clear that phonon-assisted transitions between polariton states are permitted through the interaction term $\alpha\beta V(p_1^\dagger p_2 + p_2^\dagger p_1)$. Concentrating on this term, the contribution of real phonon-assisted transitions $\Gamma_{\rm ph}$ to the polariton broadening $\Gamma_{1,2}$ can be understood in terms of Fermi's golden rule (FGR) [32],

$$\Gamma_{\rm ph} = \pi N_{\pm\Delta\omega/v_s} \sum_q |\alpha\beta\lambda_q|^2 \delta(\pm\Delta\omega - \omega_q), \tag{33}$$

where $\lambda_q$ is the matrix element of the exciton-phonon coupling for the $q$th phonon mode, $v_s$ is the speed of sound in the material, $\Delta\omega$ is the polariton Rabi splitting, and $N_{\pm\Delta\omega/v_s}$ is the Bose distribution function [Eq. (E3)] evaluated at $q = \pm\Delta\omega/v_s$. We take the positive (negative) value of $\Delta\omega$ in Eq. (33) for the $1 \to 2$ ($2 \to 1$) polariton transition.

Taking the average polariton Rabi splitting $\Delta\omega$ of $2g$ and approximating $\alpha$ and $\beta$ as $\alpha \approx \beta \approx 1/\sqrt{2}$ (valid in the case of zero detuning or, more generally, in the regime $g \gg |\omega_X - \omega_C|$), we obtain the following expressions for the lower (1) and upper (2) polariton line broadenings:

$$\Gamma_1 = \Gamma_0 + N_{2g/v_s}\bar{\Gamma}_{\rm ph}, \tag{34}$$

$$\Gamma_2 = \Gamma_0 + (N_{2g/v_s} + 1)\bar{\Gamma}_{\rm ph}, \tag{35}$$

where $\Gamma_0 = 1/2(\gamma_X + \gamma_C)$ is the intrinsic line broadening due to the long-time ZPL dephasing $\gamma_X$ and radiative decay $\gamma_C$, and, for a spherical Gaussian QD model (see Appendix F), $\bar{\Gamma}_{\rm ph}$ has the form

$$\bar{\Gamma}_{\rm ph} = \frac{g^3(D_c - D_v)^2}{2\pi\rho_m v_s^5} \exp\left(-\frac{2g^2 l^2}{v_s^2}\right), \tag{36}$$

where the material-dependent parameters $D_{c(v)}$, $\rho_m$ and $v_s$ are, respectively, the deformation potential of the conduction (valence) band, the mass density, and the speed of sound.

The linewidths $\Gamma_{1,2}$ calculated using FGR, Eqs. (34) and (35), are shown alongside the Trotter decomposition results in the lower panel of Fig. 3. There is, in general, remarkable agreement between FGR and the results obtained from the $L$N Trotter decomposition method; the small discrepancies may be attributed to multi-phonon transitions, which are not accounted for in FGR.

The inset in Fig. 2(b) demonstrates the quality of the present calculation at $g = 0.6$ meV. For the values of $L$ shown, the error for the parameters of the long-time dependence Eq. (30) decreases exponentially as $2^{-L/2}$. The computational time $t_c$ is $\propto 2^L$, giving an error that scales as $1/\sqrt{t_c}$. Even for large $g$, the $L$N result quickly converges to the exact solution, with the relative error of the polariton linewidths $\Gamma_{1,2}$ saturating at a level below 1%, as shown in Appendix I.

## VI. CONCLUSION

We have provided an asymptotically exact semianalytic solution for the linear optical response of a quantum dot-microcavity system coupled to an acoustic phonon environment, valid for a wide range of system parameters. Even for large cavity-quantum dot coupling strength $g$, this solution reveals the dephasing mechanism in terms of real phonon-assisted transitions between polariton states of the Rabi doublet. For small $g$, our approach simplifies to an accurate analytic solution which provides an intuitive physical picture in terms of polaron-transformed polariton states superimposed with the phonon broadband, known from the independent boson model.

## ACKNOWLEDGMENT

The authors acknowledge support by the EPSRC under the DTA scheme and Grant No. EP/M020479/1.

## APPENDIX A: DERIVATION OF EQ. (7) FOR THE LINEAR POLARIZATION

We take as our starting point the standard definition of the optical polarization,

$$P(t) = \mathrm{Tr}\{\rho(t)c\}, \tag{A1}$$

where the annihilation operator $c$ stands either for the exciton operator $d$ or for the cavity operator $a$. Consequently, Eq. (A1) has the meaning of the full excitonic or photonic polarization, respectively. Here $\rho(t)$ is the full density matrix of the system, including the exciton, cavity, and phonon degrees of freedom.

To obtain the *linear* polarization from Eq. (A1), we first need to assume a pulsed excitation of the system at time $t = 0$, which is described by the following evolution of the density matrix,

$$\rho(0_+) = e^{-i\mathcal{V}}\rho(-\infty)e^{i\mathcal{V}}, \tag{A2}$$

where $\rho(-\infty)$ is the density matrix of a fully unexcited system, with its exciton-cavity part being in the absolute ground state $|0\rangle$ and phonons being in thermal equilibrium,

$$\rho(-\infty) = |0\rangle\langle 0|\rho_0, \tag{A3}$$

$$\rho_0 = e^{-\beta H_{\rm ph}}/\mathrm{Tr}\{e^{-\beta H_{\rm ph}}\}_{\rm ph}. \tag{A4}$$

Here, $\beta = (k_B T)^{-1}$, and the trace is taken over all possible phonon states. The perturbation $\mathcal{V}$ due to the pulsed excitation has the form

$$\mathcal{V} = \alpha(\tilde{c}^\dagger + \tilde{c}), \tag{A5}$$

where $\alpha$ is a constant, and again, $\tilde{c}$ is either $d$ or $a$, depending on the excitation (feeding) channel.

We assume that the evolution of the full density matrix of the exciton-cavity-phonon system after its optical pulsed excitation is given by the following standard Lindblad master equation:

$$\begin{aligned} i\dot{\rho} = {} & [\mathcal{H}, \rho] + i\gamma_X(2d\rho d^\dagger - d^\dagger d\rho - \rho d^\dagger d) \\ & + i\gamma_C(2a\rho a^\dagger - a^\dagger a\rho - \rho a^\dagger a), \end{aligned} \tag{A6}$$

in which the Hamiltonian $\mathcal{H} = \mathcal{H}_{\rm JC} + H_{IB}$ is *Hermitian*. Here, $\mathcal{H}_{\rm JC}$ is the JC Hamiltonian $H_{\rm JC}$ defined by Eq. (1) in which the complex frequencies

$$\omega_{X,C} = \Omega_{X,C} - i\gamma_{X,C}, \quad \Omega_{X,C}, \gamma_{X,C} \in \mathbb{R}, \tag{A7}$$

are replaced by real ones by removing the imaginary parts: $\omega_{X,C} \to \Omega_{X,C}$. Noting that

$$\begin{aligned} [\mathcal{H}, \rho] = {} & H\rho - \rho H^* + i\gamma_X(d^\dagger d\rho + \rho d^\dagger d) \\ & + i\gamma_C(a^\dagger a\rho + \rho a^\dagger a), \end{aligned}$$

where $H$ is the full *non-Hermitian* Hamiltonian defined on the first page of the main text and $H^*$ is its complex conjugate, we may re-express the Lindblad master equation as

$$i\dot{\rho} = H\rho - \rho H^* + 2i\gamma_X d\rho d^\dagger + 2i\gamma_C a\rho a^\dagger. \tag{A8}$$

In the linear polarization, we keep in the full polarization only the terms which are linear in $\alpha$. Looking closer, this implies keeping only $|X\rangle\langle 0|$ and $|C\rangle\langle 0|$ elements of the density matrix. When the density matrix is reduced to only $|X\rangle\langle 0|$ and $|C\rangle\langle 0|$ elements, the last two terms in Eq. (A8) vanish, which yields an explicit solution,

$$\rho(t) = e^{-iHt}\rho(0_+)e^{iH^*t}, \tag{A9}$$

in which $H^*$ can actually be replaced by $H_{\rm ph}$. The linear polarization then takes the form

$$P_L(t) = -i\alpha\mathrm{Tr}\{e^{-iHt}\tilde{c}^\dagger|0\rangle\langle 0|\rho_0 e^{iH_{\rm ph}t}c\}. \tag{A10}$$

Now, dropping the unimportant constant factor $-i\alpha$ and introducing indices $j, k = X, C$ to replace the operators $\tilde{c}^\dagger$ and $c$, we arrive at Eqs. (7) of the main text.

## APPENDIX B: TROTTER DECOMPOSITION OF THE EVOLUTION OPERATOR

Using the Trotter decomposition, the evolution operator is presented in Eq. (8) as $\hat{U}(t) = \lim_{N\to\infty}\hat{U}_N(t)$, where

$$\begin{aligned} \hat{U}_N(t) = {} & e^{iH_{\rm ph}t}e^{-iH_{\rm IB}(t-t_{N-1})}e^{-iH_{\rm JC}(t-t_{N-1})}\cdots \\ & \times e^{-iH_{\rm IB}(t_n-t_{n-1})}e^{-iH_{\rm JC}(t_n-t_{n-1})}\cdots \\ & \times e^{-iH_{\rm IB}t_1}e^{-iH_{\rm JC}t_1} \\ = {} & e^{iH_{\rm ph}t}e^{-iH_{\rm IB}(t-t_{N-1})}e^{-iH_{\rm ph}t_{N-1}}e^{-iH_{\rm JC}(t-t_{N-1})}\cdots \\ & \times e^{iH_{\rm ph}t_n}e^{-iH_{\rm IB}(t_n-t_{n-1})}e^{-iH_{\rm ph}t_{n-1}}e^{-iH_{\rm JC}(t_n-t_{n-1})}\cdots \\ & \times e^{iH_{\rm ph}t_1}e^{-iH_{\rm IB}t_1}e^{-iH_{\rm JC}t_1} \\ = {} & \hat{W}(t, t_{N-1})\hat{M}(t-t_{N-1})\cdots \\ & \times \hat{W}(t_n, t_{n-1})\hat{M}(t_n-t_{n-1})\cdots\hat{W}(t_1, 0)\hat{M}(t_1), \end{aligned} \tag{B1}$$

where we have used the fact that the operators $H_{\rm ph}$ and $H_{\rm JC}$ commute. From the definition of $H_{\rm IB}$, we note that

$$\hat{W}(t_n, t_{n-1}) = e^{iH_{\rm ph}t_n}e^{-iH_{\rm IB}(t_n-t_{n-1})}e^{-iH_{\rm ph}t_{n-1}} \tag{B2}$$

is a diagonal operator in the two-basis state matrix representation in terms of $|X\rangle$ and $|C\rangle$:

$$\hat{W}(t_n, t_{n-1}) = \begin{pmatrix} W_X(t_n, t_{n-1}) & 0 \\ 0 & W_C(t_n, t_{n-1}) \end{pmatrix} \tag{B3}$$

with

$$\begin{aligned} & W_X(t_n, t_{n-1}) = e^{iH_{\rm ph}t_n}e^{-i(H_{\rm ph}+V)(t_n-t_{n-1})}e^{-iH_{\rm ph}t_{n-1}}, \\ & W_C(t_n, t_{n-1}) = 1. \end{aligned}$$

Using the time-ordering operator $\mathcal{T}$, $\hat{W}$-matrix element $W_X$ can be written as

$$W_X(t_n, t_{n-1}) = \mathcal{T}\exp\left\{-i\int_{t_{n-1}}^{t_n} V(\tau)d\tau\right\}, \tag{B4}$$

where $V(\tau) = e^{iH_{\rm ph}\tau}Ve^{-iH_{\rm ph}\tau}$ is the interaction representation of the exciton-phonon coupling $V$, which is given by Eqs. (4) of the main text.

Substituting the evolution operator Eq. (B1) into Eqs. (7) for the polarization $P_{jk}(t)$ and explicitly expressing the matrix products gives

$$\begin{aligned} P_{jk}(t) = {} & \sum_{i_{N-1}=X,C}\cdots\sum_{i_1=X,C}\langle W_{i_N}M_{i_N i_{N-1}} \\ & \times W_{i_{N-1}}M_{i_{N-1}i_{N-2}}\cdots M_{i_{n+1}i_n}W_{i_n}M_{i_n i_{n-1}}\cdots W_{i_1}M_{i_1 i_0}\rangle_{\rm ph} \end{aligned} \tag{B5}$$

with $i_N = j$ and $i_0 = k$. From here, we note that only $W$ elements contain the phonon interaction and through a simple rearrangement of Eq. (B5) we arrive at Eq. (12) of the main text.

## APPENDIX C: LINEAR POLARIZATION IN THE NN APPROXIMATION, INCLUDING AN EXAMPLE REALIZATION

The single summation in the cumulant Eq. (19) allows us to express, for each realization, the expectation value in Eq. (12) as a product:

$$\begin{aligned}\langle W_{i_N}(t,t_{N-1})\cdots W_{i_n}(t_n,t_{n-1})\cdots W_{i_2}(t_2,t_1)W_{i_1}(t_1,0)\rangle_{\rm ph}\\ = e^{\delta_{i_N X}K_0}e^{\delta_{i_{N-1}X}(K_0+2\delta_{i_N X}K_1)}\cdots\\ \times e^{\delta_{i_{n-1}X}(K_0+2\delta_{i_n X}K_1)}\cdots e^{\delta_{i_1 X}(K_0+2\delta_{i_2 X}K_1)}.\end{aligned} \tag{C1}$$

It is convenient to introduce

$$R_{i_n i_{n-1}} = e^{\delta_{i_{n-1}X}(K_0+2\delta_{i_n X}K_1)}, \tag{C2}$$

enabling us to express the expectation values of the product of $W$ operators for a given realization Eq. (C1) as $e^{\delta_{i_N X}K_0}R_{i_N i_{N-1}}\cdots R_{i_2 i_1}$. Inserting this expression into Eq. (12), we find

$$\begin{aligned}P_{jk}(t) = e^{\delta_{i_N X}K_0}\sum_{i_{N-1}=X,C}\cdots\sum_{i_1=X,C}(M_{i_N i_{N-1}}\cdots M_{i_2 i_1}M_{i_1 i_0})\\ \times(R_{i_N i_{N-1}}\cdots R_{i_2 i_1}).\end{aligned} \tag{C3}$$

We then join together corresponding $M_{i_n i_{n-1}}$ and $R_{i_n i_{n-1}}$ elements through the definition of a matrix

$$G_{i_n i_{n-1}} = M_{i_n i_{n-1}}R_{i_n i_{n-1}}, \tag{C4}$$

which transforms Eq. (C3) to

$$\begin{aligned}P_{jk}(t) = e^{\delta_{i_N X}K_0}\sum_{i_{N-1}=X,C}\cdots\sum_{i_{n-1}=X,C}\cdots\\ \times\sum_{i_1=X,C}G_{i_N i_{N-1}}\cdots G_{i_n i_{n-1}}\cdots G_{i_2 i_1}M_{i_1 i_0}.\end{aligned} \tag{C5}$$

Using the fact that $i_N = j$ and $i_0 = k$, we arrive at Eq. (20), which is compactly represented in Eq. (22) as a product of matrices.

To illustrate this idea by way of an example, we take a particular realization for $N = 5$, provided for illustration in Fig. 4. In this realization, $i_1 = X$, $i_2 = C$, $i_3 = X$, $i_4 = X$, and $i_5 = C$. Each exponential $e^{\delta_{i_{n-1}X}(K_0+2\delta_{i_n X}K_1)}$ in Eq. (C1) can be visualized as an L-shaped portion of the time grid (color coded in the figure). In the illustrated realization we have,

$$\begin{aligned}R_{i_2 i_1} &= e^{\delta_{i_1 X}(K_0+2\delta_{i_2 X}K_1)} = e^{K_0},\\ R_{i_3 i_2} &= e^{\delta_{i_2 X}(K_0+2\delta_{i_3 X}K_1)} = e^{0} = 1,\\ R_{i_4 i_3} &= e^{\delta_{i_3 X}(K_0+2\delta_{i_4 X}K_1)} = e^{K_0+2K_1},\\ R_{i_5 i_4} &= e^{\delta_{i_4 X}(K_0+2\delta_{i_5 X}K_1)} = e^{K_0},\\ e^{\delta_{i_5 X}K_0} &= e^{0} = 1.\end{aligned}$$

We then find

$$\begin{aligned}G_{i_2 i_1} &= G_{CX} = M_{CX}e^{K_0},\\ G_{i_3 i_2} &= G_{XC} = M_{XC},\\ G_{i_4 i_3} &= G_{XX} = M_{XX}e^{K_0+2K_1},\\ G_{i_5 i_4} &= G_{CX} = M_{CX}e^{K_0},\end{aligned}$$

which contributes to the total polarization Eq. (C5).

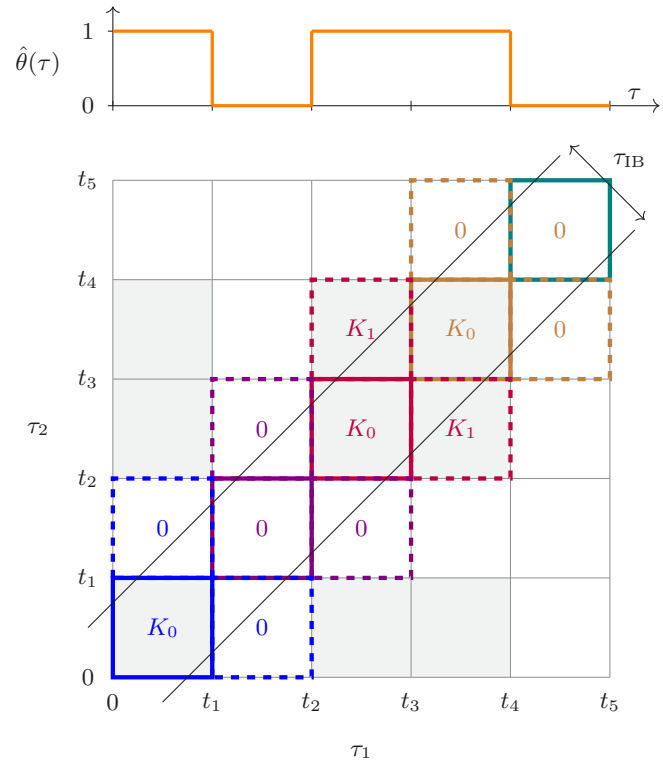


FIG. 4. Example realization for the NN implementation with $N = 5$. In this realization, $i_1 = X$, $i_2 = C$, $i_3 = X$, $i_4 = X$, $i_5 = C$, as is clear from the step function $\hat{\theta}(t)$ associated with the given realization, shown on the top.

Note that the condition for the NN approximation to be valid is also illustrated in Fig. 4: All the time moments of integration for which $|\tau_2 - \tau_1| < \tau_{\rm IB}$ should be located within the colored squares, which are taken into account in the NN calculation of the cumulant.

## APPENDIX D: CALCULATION OF $K_{|n-m|}$ FROM THE IB MODEL CUMULANT

As is clear from the definition given in Eq. (18) of the main text, the integral $K_{|n-m|}$ depends only on the difference $|n - m|$. To find $K_0$, which is depicted graphically in Fig. 5(a), we set $m = n = 1$,

$$K_0 = -\frac{1}{2}\int_0^{t_1}d\tau_1\int_0^{t_1}d\tau_2\langle\mathcal{T}V(\tau_1)V(\tau_2)\rangle = K(\Delta t), \tag{D1}$$

where $K(t)$ is the IB cumulant, calculated explicitly in Appendix E below, see Eq. (E5).

Analogously, to find $K_1$ we may set $m = 1$ and $n = 2$, which gives

$$K_1 = -\frac{1}{2}\int_{t_1}^{t_2}d\tau_1\int_0^{t_1}d\tau_2\langle\mathcal{T}V(\tau_1)V(\tau_2)\rangle, \tag{D2}$$

or, by setting $m = 2$ and $n = 1$ instead, we obtain the same result:

$$K_1 = -\frac{1}{2}\int_0^{t_1}d\tau_1\int_{t_1}^{t_2}d\tau_2\langle\mathcal{T}V(\tau_1)V(\tau_2)\rangle. \tag{D3}$$

Equations (D2) and (D3) correspond to the squares labeled as $K_1$ in Fig. 5(b). To calculate $K_1$ from the IB cumulant, we note that

$$K(2\Delta t) = 2K_0 + 2K_1. \tag{D4}$$

Therefore,

$$K_1 = \tfrac{1}{2}[K(2\Delta t) - 2K_0]. \tag{D5}$$

In general, all the integrals $K_p$ can be found recursively:

$$K_{p>0} = \frac{1}{2}\Bigg[K((p+1)\Delta t) - (p+1)K_0 - \sum_{q=1}^{p-1} 2(p+1-q)K_q\Bigg]. \tag{D6}$$

For all $t < \tau_{\mathrm{IB}}$, we modify our approach by replacing our fixed $\Delta t$ with variable $\Delta t' = t/(L+1)$, where $L$ is the chosen number of neighbors. Accordingly, in this regime time is discretized into $L+1$ tranches. For example, the NN ($L=1$) approach uses a $2 \times 2$ grid, as shown in Fig. 6. Crucially, this ensures that no portions of the $K(t)$ grid are neglected. We therefore may allow $\Delta t'$ to become arbitrarily small whilst always exactly calculating $K(t)$. Note that this is only valid for $t < \tau_{\mathrm{IB}}$: If we were to extend this approach to $t > \tau_{\mathrm{IB}}$, then for some values of $t$ our time interval $\Delta t'$ would become too large, and the accuracy of the calculation would be degraded.

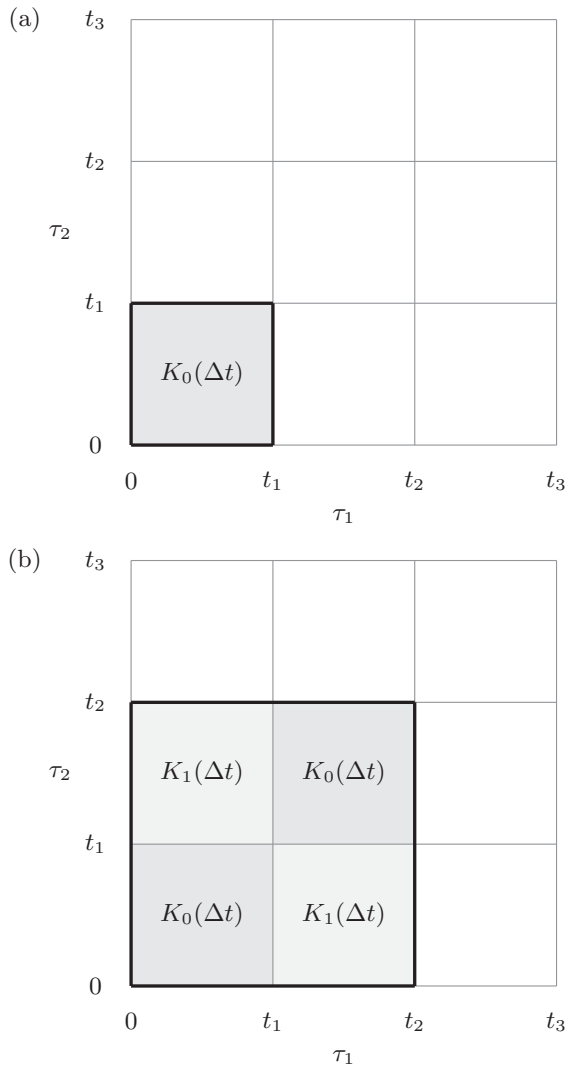


FIG. 5. Graphical representations of the use of the IB model cumulant $K(t)$ for finding (a) $K_0(\Delta t)$ and (b) $K_1(\Delta t)$.

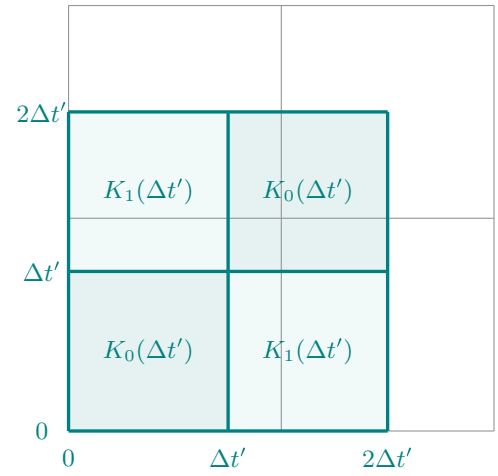


FIG. 6. Adaptation of the grid of Fig. 5 for small time: $t < \tau_{\mathrm{IB}}$. The grey grid illustrates the $\Delta t$ discretization used for $t > \tau_{\mathrm{IB}}$ (as shown in Fig. 5), while the green grid illustrates the adapted discretization for $t < \tau_{\mathrm{IB}}$. In this small time regime and the $L = 1$ implementation, a $2 \times 2$ grid is always used, giving $\Delta t' = t/2$. More generally, the $L$N implementation requires a grid of size $(L+1) \times (L+1)$ for $t < \tau_{\mathrm{IB}}$.

## APPENDIX E: THE IB MODEL CUMULANT AND ITS LONG-TIME BEHAVIOR, EQ. (24)

The IB model cumulant $K(t)$ can be conveniently written in terms of the standard phonon propagator $D_q$ [25],

$$K(t) = -\frac{i}{2}\int_0^t d\tau_1 \int_0^t d\tau_2 \sum_q |\lambda_q|^2 D_q(\tau_1 - \tau_2), \tag{E1}$$

where

$$\begin{aligned} iD_q(t) &= \langle \mathcal{T}[b_q(t) + b_{-q}^\dagger(t)]^\dagger [b_q(0) + b_{-q}^\dagger(0)]\rangle \\ &= N_q e^{i\omega_q|t|} + (N_q+1)e^{-i\omega_q|t|} \end{aligned} \tag{E2}$$

and $N_q$ is the Bose distribution function,

$$N_q = \frac{1}{e^{\beta\omega_q} - 1}. \tag{E3}$$

Performing the integration in Eq. (E1), we obtain

$$K(t) = \sum_q |\lambda_q|^2 \left(\frac{N_q}{\omega_q^2}[e^{i\omega_q t} - 1] + \frac{N_q+1}{\omega_q^2}[e^{-i\omega_q t} - 1] + \frac{it}{\omega_q}\right). \tag{E4}$$

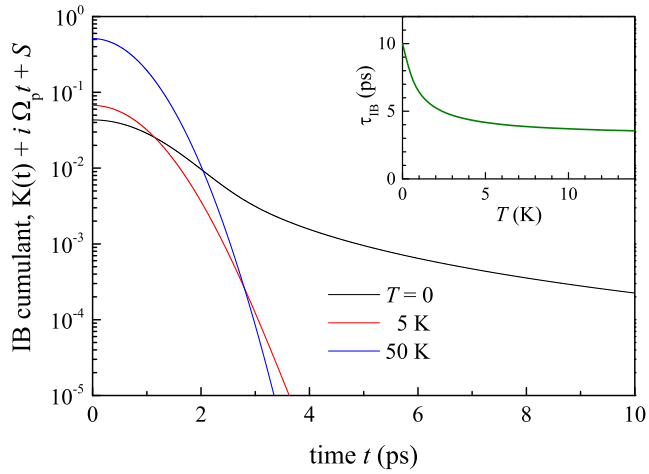


FIG. 7. IB model cumulant $K(t)$, with its long-time asymptotics $-i\Omega_p t - S$ subtracted, as a function of time $t$ for different temperatures as given. The parameters used are listed at the end of Appendix F. Inset: The phonon memory time $\tau_{\rm IB}$ playing the role of the cutoff parameter in calculation of the cumulants for different realizations in the $L$N approach.

Converting the summation over $q$ to an integration $\sum_q \to \frac{\mathbb{V}}{(2\pi)^3 v_s^3}\int d^3\omega$ (where $\mathbb{V}$ is the sample volume) and noting that $|\lambda_q|^2$ may be expressed in terms of the spectral density function $J(\omega)$ [see Eq. (F5) in Appendix F below], we rewrite Eq. (E4) as

$$K(t) = \int_0^\infty d\omega\, J(\omega)\left(\frac{N_q}{\omega^2}[e^{i\omega t} - 1] + \frac{N_q + 1}{\omega^2}[e^{-i\omega t} - 1] + \frac{it}{\omega}\right). \tag{E5}$$

In the long-time limit, Eq. (E5) simplifies to

$$K(t \to \infty) = -i\Omega_p t - S, \tag{E6}$$

with the polaron shift,

$$\Omega_p = -\int_0^\infty d\omega\, \frac{J(\omega)}{\omega}, \tag{E7}$$

and the Huang-Rhys factor,

$$S = \int_0^\infty d\omega\, \frac{J(\omega)}{\omega^2}(2N_q + 1) = \int_0^\infty d\omega\, \frac{J(\omega)}{\omega^2}\coth\left(\frac{\omega}{2k_B T}\right). \tag{E8}$$

Figure 7 shows the cumulant function $K(t)$ of the IB model with the asymptotic behavior $-i\Omega_p t - S$ subtracted. The polaron timescale $\tau_{\rm IB}$ is the time taken for the remaining part of the cumulant, $K(t) + i\Omega_p t + S$, to drop below a certain threshold value. The choice of this threshold is dictated by the accuracy required in the calculation: $\tau_{\rm IB}$ determines the choice of the minimal time step in the NN approximation ($\Delta t \approx \tau_{\rm IB}$) and the $L$N approach ($L\Delta t \approx \tau_{\rm IB}$), and any contributions from the quickly decaying part of the cumulant $K(t) + i\Omega_p t + S$ beyond $t = \tau_{\rm IB}$ are neglected in the calculation. Choosing a threshold of $\sim 10^{-4}$, we see from Fig. 7 that the polaron timescale $\tau_{\rm IB}$ is approximately 3.25 ps at $T = 5$ and $T = 50$ K for the realistic QD parameters used in the calculation (see Appendix F). This timescale is, however, strongly dependent on the exciton confinement length $l$ and speed of sound in the material $v_s$ (set to 3.3 nm and $4.6 \times 10^3$ m/s, respectively, to produce Fig. 7). We therefore define, in Eq. (6) of the main text, $\tau_{\rm IB}$ in terms of these key parameters.

At very low temperatures, $\tau_{\rm IB}$ also becomes temperature-dependent, as is clear from Fig. 7; in the present case $\tau_{\rm IB}$ increases to 10 ps at $T = 0$. The full temperature dependence of $\tau_{\rm IB}$ is shown up to $T = 14$ K in the inset of Fig. 7.

## APPENDIX F: EXCITON-PHONON COUPLING MATRIX ELEMENT $\lambda_q$ AND THE SPECTRAL DENSITY FUNCTION $J(\omega)$

At low temperatures, the exciton-phonon interaction is dominated by the deformation potential coupling to longitudinal acoustic phonons. Assuming (i) that the phonon parameters in the confined QD do not differ significantly from those in the surrounding material and (ii) that the acoustic phonons have linear dispersion $\omega_q = v_s|q|$, where $v_s$ is the sound velocity in the material, the matrix coupling element $\lambda_q$ is given by

$$\lambda_q = \frac{q\mathcal{D}(q)}{\sqrt{2\rho_m \omega_q \mathbb{V}}}, \tag{F1}$$

where $\rho_m$ is the mass density of the material. Assuming a factorizable form of the exciton wave function, $\Psi_X(\mathbf{r}_e, \mathbf{r}_h) = \psi_e(\mathbf{r}_e)\psi_h(\mathbf{r}_h)$, where $\psi_{e(h)}(\mathbf{r})$ is the confined electron (hole) ground state wave function, the form-factor $\mathcal{D}(q)$ is given by

$$\mathcal{D}(q) = \int d\mathbf{r}[D_v|\psi_h(\mathbf{r})|^2 - D_c|\psi_e(\mathbf{r})|^2]e^{-i\mathbf{q}\cdot\mathbf{r}}, \tag{F2}$$

with $D_{c(v)}$ being the material-dependent deformation potential constant for the conduction (valence) band. We choose for simplicity spherically symmetric parabolic confinement potentials which give Gaussian ground-state wave functions,

$$\psi_{e(h)}(\mathbf{r}) = \frac{1}{(\sqrt{\pi} l_{e(h)})^{3/2}} \exp\left(-\frac{r^2}{2l_{e(h)}^2}\right), \tag{F3}$$

and thus

$$\lambda_q = \sqrt{\frac{q}{2\rho_m v_s \mathbb{V}}}(D_v - D_c)\, e^{-\frac{l^2 q^2}{4}}, \tag{F4}$$

taking the case of $l_e = l_h = l$ for simplicity.

The spectral density $J(\omega)$ is defined as

$$J(\omega) = \sum_q |\lambda_q|^2 \delta(\omega - \omega_q). \tag{F5}$$

This is equivalent to taking the product of $|\lambda_q|^2$ with the density of states in $\omega$-space. Switching from the summation to an integration, as in Eq. (E5), the spectral density becomes

$$J(\omega) = |\lambda_q|^2 \frac{2\mathbb{V}}{(2\pi)^2 v_s^3}\omega^2 = \frac{\omega^3 (D_c - D_v)^2}{4\pi^2 \rho_m v_s^5} e^{-\frac{\omega^2}{\omega_0^2}}, \tag{F6}$$

where $q = \omega/v_s$ and $\omega_0 = \sqrt{2}v_s/l$ is the so-called cut-off frequency; it is inversely related to the phonon memory time, $\tau_{\rm IB} \approx 2\pi/\omega_0$, leading to Eq. (6).

In all calculations, we use $l = 3.3\,\mathrm{nm}$, $D_c - D_v = -6.5\,\mathrm{eV}$, $v_s = 4.6 \times 10^3$ m/s, and $\rho_m = 5.65\ \mathrm{g/cm^3}$.

## APPENDIX G: LONG-TIME ANALYTICS FOR THE LINEAR POLARIZATION

In this section, we derive the approximate analytic result Eqs. (25) and (26) for the linear polarization $\hat{P}(t)$ in the long-time limit. This approximation is valid for small values of the exciton-cavity coupling strength $g$, which guarantees that the polariton timescale is much longer than the phonon memory time, $\tau_{\mathrm{JC}} \gg \tau_{\mathrm{IB}}$. As a starting point, we take the result for $\hat{P}(t)$ in the NN approach, Eqs. (22) and (23), and use it for $\Delta t \gtrsim \tau_{\mathrm{IB}}$. This condition implies that we can take both $K_0$ and $K_1$ in the long-time limit, using the asymptotic formula Eq. (24):

$$K_0 = K(\Delta t) \approx -i\Omega_p \Delta t - S, \tag{G1}$$

$$K_1 = \frac{1}{2}(K(2\Delta t) - 2K(\Delta t)) \approx \frac{S}{2}. \tag{G2}$$

We would now like to replace the product of $N$ matrices in Eq. (22) by an approximate analytic expression, taking the Trotter limit $N \to \infty$. To do so, we initially derive explicit expressions for $\hat{M}$ and $\hat{G}$ in the two-state basis of $|X\rangle$ and $|C\rangle$. From Eq. (9), we obtain

$$\begin{pmatrix} M_{XX} & M_{XC} \\ M_{CX} & M_{CC} \end{pmatrix} = e^{-i\omega_1 \Delta t} \begin{pmatrix} 1-\beta^2\delta & -\alpha\beta\delta \\ -\alpha\beta\delta & 1-\alpha^2\delta \end{pmatrix}, \tag{G3}$$

where $\omega_{1,2}$ are the eigenvalues of the JC Hamiltonian $H_{\mathrm{JC}}$, $\delta = 1 - e^{-i(\omega_2-\omega_1)\Delta t}$, and $\alpha$ and $\beta$ make up the unitary matrices $\hat{Y}$, $\hat{Y}^{-1}$ that diagonalize $H_{\mathrm{JC}}$:

$$H_{\mathrm{JC}} = \begin{pmatrix} \omega_X & g \\ g & \omega_C \end{pmatrix} = \hat{Y}^{-1} \begin{pmatrix} \omega_1 & 0 \\ 0 & \omega_2 \end{pmatrix} \hat{Y}, \tag{G4}$$

$$\hat{Y} = \begin{pmatrix} \alpha & -\beta \\ \beta & \alpha \end{pmatrix}, \tag{G5}$$

$$\alpha = \frac{\Delta}{\sqrt{\Delta^2 + g^2}}, \tag{G6}$$

$$\beta = \frac{g}{\sqrt{\Delta^2 + g^2}}, \tag{G7}$$

$$\omega_{1,2} = \frac{\omega_X + \omega_C}{2} \mp \sqrt{g^2 + \delta_{XC}^2}, \tag{G8}$$

with $\Delta = \sqrt{\delta_{XC}^2 + g^2} - \delta_{XC}$ and $\delta_{XC} = 1/2(\omega_X - \omega_C)$. Substituting the expression for $\hat{M}$ given by Eq. (G3) into Eq. (23), and using Eqs. (G1) and (G2), we find

$$\hat{G} = \begin{pmatrix} M_{XX} e^{K_0 + 2K_1} & M_{XC} \\ M_{CX} e^{K_0} & M_{CC} \end{pmatrix} \approx e^{-i\omega_1 \Delta t} \begin{pmatrix} e^{-i\Omega_p \Delta t}(1-\beta^2\delta) & -\alpha\beta\delta \\ -e^{-i\Omega_p \Delta t - S}\alpha\beta\delta & 1-\alpha^2\delta \end{pmatrix}. \tag{G9}$$

Now we use the fact that $\Delta t \ll \tau_{\mathrm{JC}}$ (which is equivalent to $|\omega_2 - \omega_1|\Delta t \ll 1$). We also assume that the polaron shift $\Omega_p$ is small, so $|\Omega_p|\Delta t \ll 1$. Working within these limits is equivalent to taking the Trotter limit $\Delta t = t/N \to 0$. Keeping only the terms linear in $\Delta t$ in the matrix elements, we obtain

$$\hat{G} \approx e^{-i\omega_1 \Delta t}\left[\mathbb{1} - i\Delta t \begin{pmatrix} \Omega_p + \beta^2\omega_{21} & \alpha\beta\omega_{21} \\ \alpha\beta\omega_{21} e^{-S} & \alpha^2\omega_{21} \end{pmatrix}\right], \tag{G10}$$

where $\omega_{21} = \omega_2 - \omega_1$ and $\mathbb{1}$ is a $2 \times 2$ identity matrix. From Eq. (G4) and the fact that $\alpha^2 + \beta^2 = 1$, we find

$$\beta^2(\omega_2 - \omega_1) = \omega_X - \omega_1,$$
$$\alpha^2(\omega_2 - \omega_1) = \omega_C - \omega_1,$$
$$\alpha\beta(\omega_2 - \omega_1) = g.$$

This allows us to rewrite Eq. (G10) in the following way:

$$\hat{G} = e^{-i\omega_1 \Delta t}\left[\mathbb{1}(1 + i\omega_1 \Delta t) - i\Delta t \begin{pmatrix} \omega_X + \Omega_p & g \\ g e^{-S} & \omega_C \end{pmatrix}\right].$$

Now, we diagonalize $\hat{G}$,

$$\hat{G} = \hat{Z}\hat{\Lambda}\hat{Z}^{-1}, \tag{G11}$$

where the transformation matrix has the form

$$\hat{Z} = \begin{pmatrix} e^{S/2} & 0 \\ 0 & 1 \end{pmatrix} \begin{pmatrix} \tilde{\alpha} & \tilde{\beta} \\ -\tilde{\beta} & \tilde{\alpha} \end{pmatrix}, \tag{G12}$$

in which the second matrix diagonalizes a phonon-renormalized JC Hamiltonian $\tilde{H}$, as defined in Eq. (26):

$$\tilde{H} = \begin{pmatrix} \omega_X + \Omega_p & g e^{-S/2} \\ g e^{-S/2} & \omega_C \end{pmatrix} = \begin{pmatrix} \tilde{\alpha} & \tilde{\beta} \\ -\tilde{\beta} & \tilde{\alpha} \end{pmatrix} \begin{pmatrix} \tilde{\omega}_1 & 0 \\ 0 & \tilde{\omega}_2 \end{pmatrix} \begin{pmatrix} \tilde{\alpha} & -\tilde{\beta} \\ \tilde{\beta} & \tilde{\alpha} \end{pmatrix}. \tag{G13}$$

The matrix of the eigenvalues $\hat{\Lambda}$ in Eq. (G11) then takes the form

$$\hat{\Lambda} = e^{-i\omega_1 \Delta t}\left[\mathbb{1} - i\Delta t \begin{pmatrix} \tilde{\omega}_1 - \omega_1 & 0 \\ 0 & \tilde{\omega}_2 - \omega_1 \end{pmatrix}\right]. \tag{G14}$$

Coming back to the NN expression for the polarization Eq. (22),

$$\hat{P}(t) = \begin{pmatrix} e^{K_0} & 0 \\ 0 & 1 \end{pmatrix} \hat{G}^N \hat{G}^{-1} \hat{M}, \tag{G15}$$

we note that $\hat{G}^{-1} \approx \mathbb{1}$ and $\hat{M} \approx \mathbb{1}$ in the limit $\Delta t \to 0$, and also $e^{K_0} \approx e^{-S}$ (still keeping the condition $\Delta t \gtrsim \tau_{\mathrm{IB}}$). We then obtain in the long-time limit $t \gtrsim \tau_{\mathrm{IB}}$:

$$\hat{P}(t) = \begin{pmatrix} e^{-S} & 0 \\ 0 & 1 \end{pmatrix} \hat{Z}\hat{\Lambda}^N\hat{Z}^{-1}. \tag{G16}$$

Finally, we take the limit $N \to \infty$ in the expression $\hat{\Lambda}^N$, using an algebraic formula

$$\lim_{N\to\infty}\left(1 + \frac{x}{N}\right)^N = e^x.$$

Introducing

$$x = -i(\tilde{\omega}_1 - \omega_1)t,$$
$$y = -i(\tilde{\omega}_2 - \omega_1)t,$$

we find

$$\lim_{N\to\infty} \hat{\Lambda}^N = e^{-i\omega_1 t} \lim_{N\to\infty} \begin{pmatrix} 1 + \frac{x}{N} & 0 \\ 0 & 1 + \frac{y}{N} \end{pmatrix}^N = \begin{pmatrix} e^{-i\tilde{\omega}_1 t} & 0 \\ 0 & e^{-i\tilde{\omega}_2 t} \end{pmatrix}. \tag{G17}$$

Substituting Eq. (G17) into Eq. (G16) we arrive at Eq. (25) of the main text.

## APPENDIX H: REFINED FULL TIME ANALYTIC APPROACH

The analytic solution derived in Appendix G is suited only for describing the optical polarization at long times $t \gtrsim \tau_{\rm IB}$, so any information on the evolution at short times, which is responsible for the so-called phonon BB observed in the optical spectra of QDs, is missing. To improve on this, we derive a refined, purely analytic approach which properly takes into account both the short- and long-time dynamics, providing a smooth transition between the two regimes.

We again start with the general formula Eqs. (7) for the linear polarization, writing it in a matrix form using the two basis states $|X\rangle$ and $|C\rangle$:

$$\hat{P}(t) = \langle \hat{U}(t) \rangle. \tag{H1}$$

Note that the expectation value in Eq. (H1) is taken over the phonon system in thermal equilibrium, and the $2 \times 2$ evolution matrix operator $\hat{U}(t)$ has the form

$$\hat{U}(t) = e^{iH_{\rm ph}t} e^{-iHt} = e^{-iH_{\rm JC}t} e^{iH_1 t} e^{-iHt}, \tag{H2}$$

where

$$H_1 = H_{\rm JC} + H_{\rm ph}\mathbb{1}, \tag{H3}$$

$$H = H_1 + \begin{pmatrix} 1 & 0 \\ 0 & 0 \end{pmatrix} V, \tag{H4}$$

with $H_{\rm JC}$ ($H_{\rm ph}$ and $V$) defined in Eq. (1) [Eqs. (4)] of the main text. We apply the polariton transformation, defined in Eq. (G4), to the evolution operator $\hat{U}(t)$,

$$\hat{U}(t) = \hat{Y}^{-1} e^{-iH_0 t} e^{i\bar{H}_1 t} e^{-i\bar{H}t} \hat{Y}, \tag{H5}$$

where $H_0$ is a $2 \times 2$ matrix of eigenvalues of $H_{\rm JC}$,

$$H_0 = \begin{pmatrix} \omega_1 & 0 \\ 0 & \omega_2 \end{pmatrix}, \tag{H6}$$

and

$$\bar{H}_1 = \hat{Y} H_1 \hat{Y}^{-1} = H_0 + H_{\rm ph}\mathbb{1}, \tag{H7}$$

$$\bar{H} = \hat{Y} H \hat{Y}^{-1} = H_0 + H_{\rm ph}\mathbb{1} + \hat{Q}V, \tag{H8}$$

$$\hat{Q} = \hat{Y} \begin{pmatrix} 1 & 0 \\ 0 & 0 \end{pmatrix} \hat{Y}^{-1} = \begin{pmatrix} \alpha^2 & \alpha\beta \\ \alpha\beta & \beta^2 \end{pmatrix}. \tag{H9}$$

We now define a reduced evolution operator, $\bar{U}(t)$, such that Eq. (H5) may be re-expressed as

$$\hat{U}(t) = \hat{Y}^{-1} e^{-iH_0 t} \bar{U}(t) \hat{Y}. \tag{H10}$$

$\bar{U}(t)$ may be further expressed as an exponential series,

$$\bar{U}(t) = e^{i\bar{H}_1 t} e^{-i\bar{H}t} = \mathcal{T} \exp\left\{ -i \int_0^t H_{\rm int}(t') dt' \right\}, \tag{H11}$$

where

$$H_{\rm int}(t) = e^{i\bar{H}_1 t} (\bar{H} - \bar{H}_1) e^{-i\bar{H}_1 t} = \hat{Q}(t) V(t), \tag{H12}$$

with individual interaction representations of the polariton and phonon operators: $\hat{Q}(t) = e^{iH_0 t} \hat{Q} e^{-iH_0 t}$ and $V(t) = e^{iH_{\rm ph}t} V e^{-iH_{\rm ph}t}$. The expectation value of $\bar{U}(t)$ then becomes an infinite perturbation series:

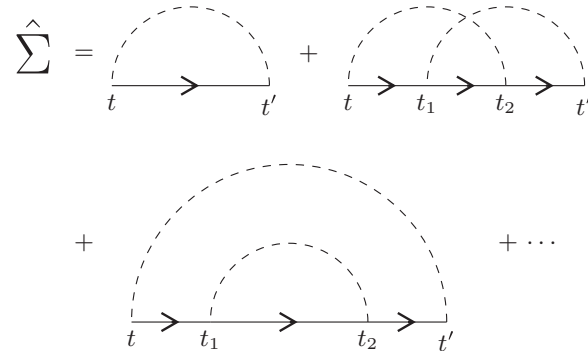


FIG. 8. Second- and fourth-order diagrams contributing to the full self energy. Solid lines with arrows (dashes lines) represent the polariton (phonon) non-interacting Green's functions.

$$\langle \bar{U}(t) \rangle = \mathbb{1} + (-i)^2 \int_0^t dt_1 \int_0^{t_1} dt_2 \hat{Q}(t_1) \hat{Q}(t_2) \langle V(t_1) V(t_2) \rangle + \cdots. \tag{H13}$$

Using Wick's theorem, all of the expectation values split into pair products. For example,

$$\begin{aligned} &\langle V(t_1) V(t_2) V(t_3) V(t_4) \rangle \\ &\quad = D(t_1 - t_2) D(t_3 - t_4) + D(t_1 - t_3) D(t_2 - t_4) \\ &\qquad + D(t_1 - t_4) D(t_2 - t_3), \end{aligned}$$

where

$$D(t - t') = \langle V(t) V(t') \rangle = \sum_q |\lambda_q|^2 i D_q(t - t')$$

is the full phonon propagator, see Eq. (E2).

It is convenient to introduce the bare polariton Green's function

$$\hat{G}^{(0)}(t) = \begin{pmatrix} G_1^{(0)}(t) & 0 \\ 0 & G_2^{(0)}(t) \end{pmatrix} = \theta(t) \begin{pmatrix} e^{-i\omega_1 t} & 0 \\ 0 & e^{-i\omega_2 t} \end{pmatrix}, \tag{H14}$$

where $\theta(t)$ is the Heaviside step function. Then the full phonon-dressed polariton Green's function $\hat{G}(t)$, which is related to the polarization matrix via

$$\hat{P}(t) = \hat{Y}^{-1} \hat{G}(t) \hat{Y}, \tag{H15}$$

satisfies the following Dyson's equation:

$$\hat{G}(t) = \hat{G}^{(0)}(t) + \int_{-\infty}^{\infty} dt_1 \int_{-\infty}^{\infty} dt_2 \times \hat{G}^{(0)}(t - t_1) \hat{\Sigma}(t_1 - t_2) \hat{G}(t_2). \tag{H16}$$

Note that this equation is equivalent to the perturbation series Eq. (H13). Here, the self-energy $\hat{\Sigma}$ is represented by all possible connected diagrams such as the second- and fourth-order diagrams sketched in Fig. 8, which are given by the

following expressions:

$$\hat{\Sigma}(t-t') = \hat{Q}\hat{G}^{(0)}(t-t')\hat{Q}D(t-t') + \int_{-\infty}^{\infty} dt_1 \int_{-\infty}^{\infty} dt_2 \times \hat{Q}\hat{G}^{(0)}(t-t_1)\hat{Q}\hat{G}^{(0)}(t_1-t_2)\hat{Q}\hat{G}^{(0)}(t_2-t')\hat{Q} \times [D(t-t_2)D(t_1-t') + D(t-t')D(t_1-t_2)] + \ldots. \quad \text{(H17)}$$

Equations (H16) and (H17) are *exact* provided that all the connected diagrams are included in the self-energy. No approximations have been used so far.

In the case of isolated (phonon-decoupled) polariton states, all of the matrices are diagonal and the problem reduces to the IB model for each polariton level, having an exact analytic solution which we exploit in our approximation. For the two phonon-coupled polariton states treated here, the exact solvability is hindered by the fact that the matrices $\hat{Q}$ and $\hat{G}^{(0)}(t)$ do not commute for any finite time $t$. However, in the timescale $|\omega_1 - \omega_2|t \ll 1$, Eq. (H14) may be approximated as $\hat{G}^{(0)}(t) \approx \theta(t)e^{-i\omega_1 t}\mathbb{1}$ and thus $\hat{G}^{(0)}(t)$ approximately commutes with $\hat{Q}$, so, for example,

$$\hat{Q}\hat{G}^{(0)}(t-t_1)\hat{Q}\hat{G}^{(0)}(t_1-t_2)\hat{Q}\hat{G}^{(0)}(t_2-t')\hat{Q} \approx \hat{Q}\hat{G}^{(0)}(t-t')\theta(t-t_1)\theta(t_1-t_2)\theta(t_2-t'),$$

using $\hat{Q}^2 = \hat{Q}$. Clearly, this approximation is valid if $\tau_{\rm JC} \gg \tau_{\rm IB}$. In this case, we obtain

$$\hat{\Sigma}(t) = \hat{Q}\begin{pmatrix} \Sigma_1(t) & 0 \\ 0 & \Sigma_2(t) \end{pmatrix}, \quad \text{(H18)}$$

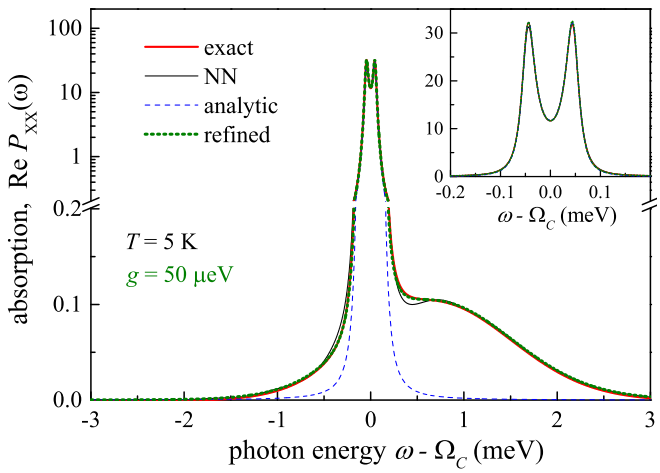


FIG. 9. Absorption spectra for $g = 50\,\mu$eV, $T = 5$ K, and zero detuning, calculated in the $LN$ approach with $L = 15$ (red thick solid lines), NN approach with $L = 1$ (black thin solid lines), long-time analytic approximation (blue dashed lines) and refined analytics (green dotted line). Other parameters used: $\Omega_X = 1329.6$ meV, $\gamma_X = 2\,\mu$eV, $\Omega_C = \Omega_X + \Omega_p$ with $\Omega_p = -49.8\,\mu$eV, and $\gamma_C = 30\,\mu$eV.

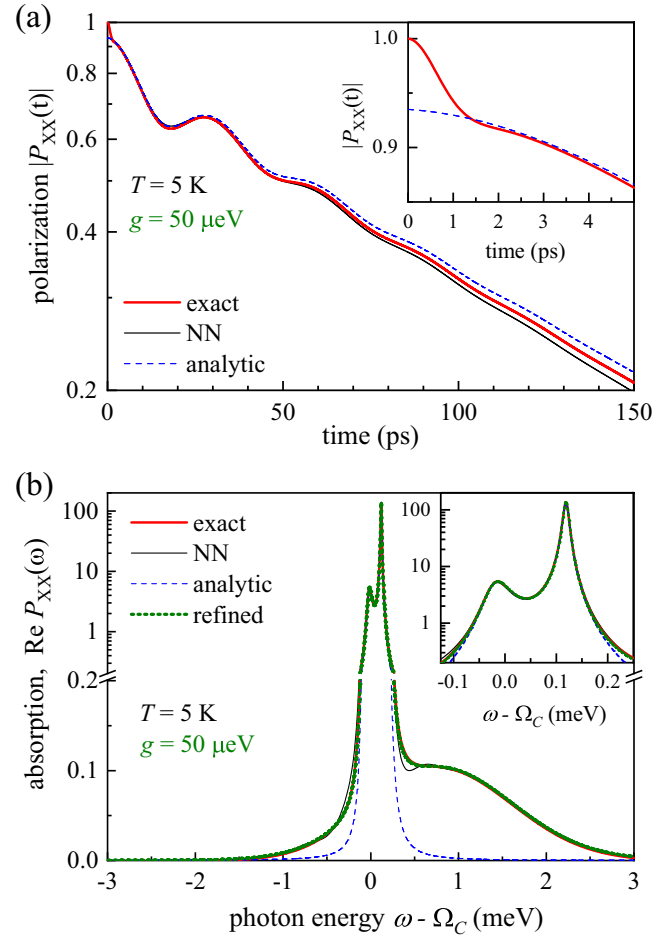


FIG. 10. (a) Excitonic linear polarization and (b) absorption for $g = 50\,\mu$eV, $T = 5$ K, and nonzero detuning, calculated in the $LN$ approach with $L = 15$ (red thick solid lines), NN approach with $L = 1$ (black thin solid lines), analytic approximation (blue dashed lines) and refined analytics (green dotted line). Other parameters used: $\Omega_X = 1329.6$ meV, $\gamma_X = 2\,\mu$eV, $\Omega_C = 1329.45$ meV, and $\gamma_C = 30\,\mu$eV.

where $\Sigma_j(t)$ is the self-energy of an isolated polariton state $j$, which contributes to the corresponding IB model problem,

$$G_j^{\rm IB}(t) = G_j^{(0)}(t) + \int_{-\infty}^{\infty} dt_1 \int_{-\infty}^{\infty} dt_2 \times G_j^{(0)}(t-t_1)\Sigma_j(t_1-t_2)G_j^{\rm IB}(t_2), \quad \text{(H19)}$$

having the following exact solution:

$$G_j^{\rm IB}(t) = G_j^{(0)}(t)e^{K(t)}, \quad \text{(H20)}$$

where the cumulant $K(t)$ is given by Eq. (E1). Equation (H19) then allows us to find the self-energies in frequency domain

$$\Sigma_j(\omega) = \frac{1}{G_j^{(0)}(\omega)} - \frac{1}{G_j^{\rm IB}(\omega)}, \quad \text{(H21)}$$

where $\Sigma_j(\omega)$, $G_j^{(0)}(\omega)$, and $G_j^{\rm IB}(\omega)$ are the Fourier transforms of $\Sigma_j(t)$, $G_j^{(0)}(t)$, and $G_j^{\rm IB}(t)$, respectively. The full matrix Green's function (and hence the polarization) is then obtained

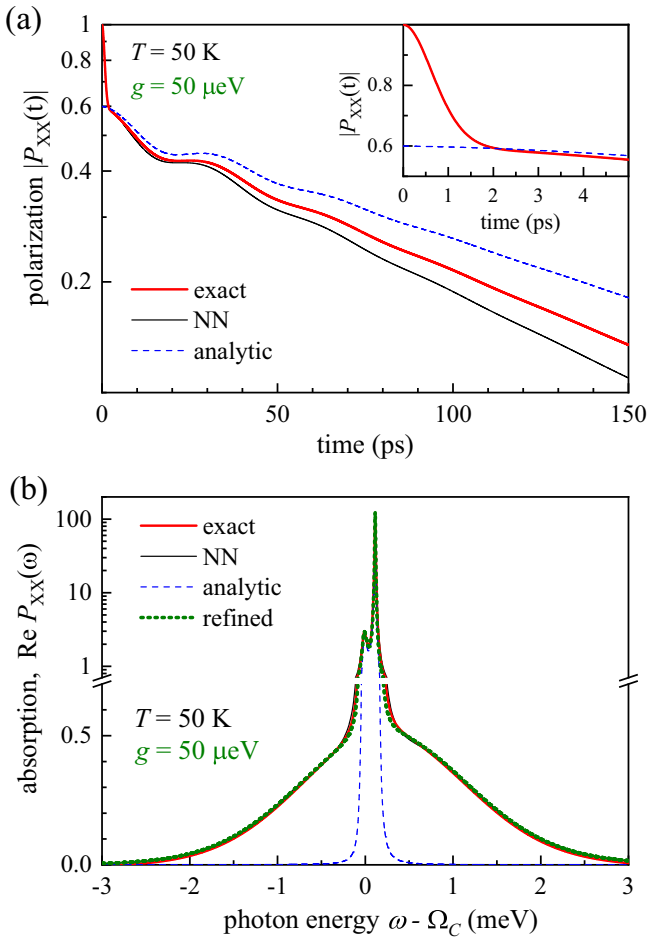


FIG. 11. As Fig. 10 but for $T = 50$ K.

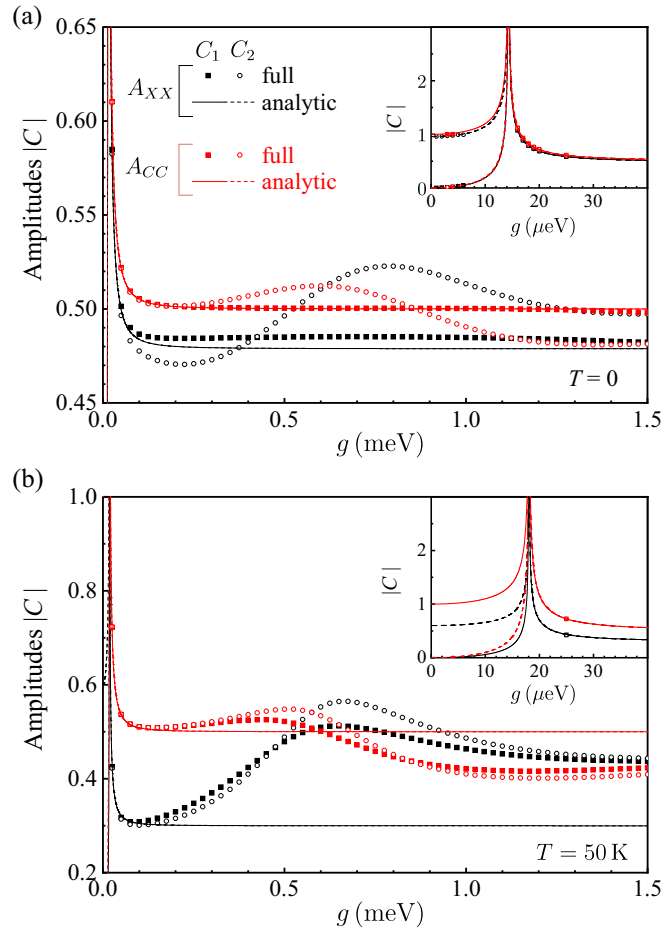


FIG. 12. Polariton amplitude coefficient $|C_1|$ ($|C_2|$) as a function of the quantum-dot–cavity coupling strength $g$ for (a) $T = 0$ and (b) $T = 50$ K shown for the full calculation by full squares (open circles) and for the long-time analytic model by full (dashed) lines. Insets zoom in on the region of small $g$, where the analytic model predicts significant changes of the amplitudes with $g$.

by solving Dyson's equation (H16) in frequency domain:

$$\hat{G}(\omega) = [\mathbb{1} - \hat{G}^{(0)}(\omega)\hat{\Sigma}(\omega)]^{-1}\hat{G}^{(0)}(\omega), \tag{H22}$$

where $\hat{G}^{(0)}$ and $\hat{\Sigma}$ are given, respectively, by Eqs. (H14) and (H18), with self-energy components provided via Eq. (H21) by the IB model solution Eq. (H20).

An obvious drawback of the above analytic model is that it does not show any phonon-induced renormalization of the exciton-cavity coupling due to the interaction with the phonon bath. This is a consequence of the present approach not properly taking into account the cumulative effect of self-energy diagrams of higher order, for which the approximate commutation of matrices $\hat{Q}$ and $\hat{G}^{(0)}(t)$ is not valid. But we know from the IB model that its exact solution in the form of a cumulant includes a nonvanishing contribution of all higher-order diagrams of the self-energy series (for realistic phonon parameters of semiconductor QDs). This significant problem can, however, be easily healed through use of the large-time asymptotics obtained in Appendix G. We introduce *by hand* one minor correction—we replace the exciton-cavity coupling $g$ in the bare JC Hamiltonian by the renormalized coupling strength $ge^{-S/2}$ in the following way:

$$H_{\rm JC} = \begin{pmatrix} \omega_X & g \\ g & \omega_C \end{pmatrix} \to \begin{pmatrix} \omega_X & ge^{-S} \\ g & \omega_C \end{pmatrix}. \tag{H23}$$

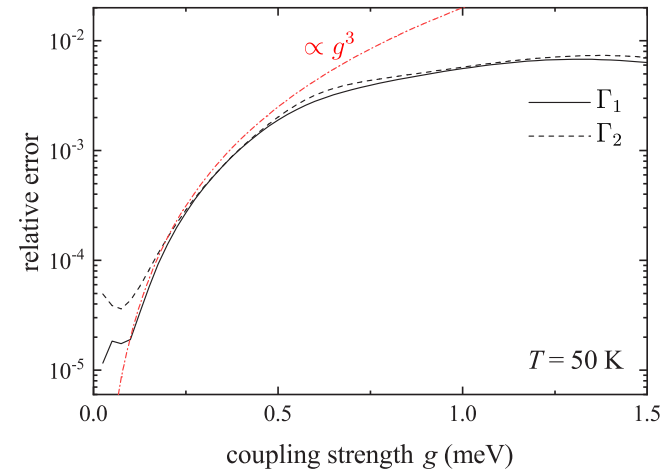


FIG. 13. Estimated relative error in polariton state linewidths $\Gamma_{1,2}$ at $T$=50 K, using the $L$N approach with $L = 13$, 14, and 15.

As in Eq. (H15), we can express the Fourier transform of the polarization as

$$\hat{P}(\omega) = \begin{pmatrix} e^{-S/2} & 0 \\ 0 & 1 \end{pmatrix} \begin{pmatrix} \bar{\alpha} & \bar{\beta} \\ -\bar{\beta} & \bar{\alpha} \end{pmatrix} \hat{\bar{G}}(\omega) \times \begin{pmatrix} \bar{\alpha} & -\bar{\beta} \\ \bar{\beta} & \bar{\alpha} \end{pmatrix} \begin{pmatrix} e^{S/2} & 0 \\ 0 & 1 \end{pmatrix}, \tag{H24}$$

where the matrices containing $\bar{\alpha}$ and $\bar{\beta}$ diagonalize a symmetrized Hamiltonian $\bar{H}_{\rm JC}$:

$$\bar{H}_{\rm JC} = \begin{pmatrix} \omega_X & g e^{-S/2} \\ g e^{-S/2} & \omega_C \end{pmatrix} = \begin{pmatrix} \bar{\alpha} & \bar{\beta} \\ -\bar{\beta} & \bar{\alpha} \end{pmatrix} \begin{pmatrix} \bar{\omega}_1 & 0 \\ 0 & \bar{\omega}_2 \end{pmatrix} \begin{pmatrix} \bar{\alpha} & -\bar{\beta} \\ \bar{\beta} & \bar{\alpha} \end{pmatrix}. \tag{H25}$$

Note that the first and last matrices of Eq. (H24) arise as a result of the replacement of the adjusted Hamiltonian in Eq. (H23) with its symmetrized version $\bar{H}_{\rm JC}$. We see that $\hat{\bar{G}}(\omega)$ in Eq. (H24) is the analog of Eq. (H22) with a replacement $\alpha \to \bar{\alpha}$, $\beta \to \bar{\beta}$, $\omega_{1,2} \to \bar{\omega}_{1,2}$.

For $P_{XX}(\omega)$ and $P_{CC}(\omega)$, the solution Eq. (H24) gives the following simple explicit expressions:

$$P_{XX}(\omega) = \frac{\bar{\alpha}^2 \bar{G}_1^{(0)}(\omega) + \bar{\beta}^2 \bar{G}_2^{(0)}(\omega)}{\bar{D}(\omega)}, \tag{H26}$$

$$P_{CC}(\omega) = \left( \frac{\bar{\alpha}^2}{\bar{G}_1^{\rm IB}(\omega)} + \frac{\bar{\beta}^2}{\bar{G}_2^{\rm IB}(\omega)} \right) \frac{\bar{G}_1^{(0)}(\omega) \bar{G}_2^{(0)}(\omega)}{\bar{D}(\omega)}, \tag{H27}$$

where

$$\bar{D}(\omega) = \bar{\alpha}^2 \frac{\bar{G}_1^{(0)}(\omega)}{\bar{G}_1^{\rm IB}(\omega)} + \bar{\beta}^2 \frac{\bar{G}_2^{(0)}(\omega)}{\bar{G}_2^{\rm IB}(\omega)} \tag{H28}$$

and $\bar{G}_j^{(0)}(\omega)$ and $\bar{G}_j^{\rm IB}(\omega)$ are, respectively, the Fourier transform of $\bar{G}_j^{(0)}(t) = \theta(t) e^{-i\bar{\omega}_j t}$ and $\bar{G}_j^{\rm IB}(t) = \bar{G}_j^{(0)}(t) e^{K(t)}$.

Figures 9, 10(b), and 11(b), as well as Fig. 1(b) of the main text, demonstrate a very good agreement between the refined analytic solution and the exact result provided by the full $L$N approach (with $L = 15$). Note that in addition to the case of zero detuning at low temperature ($T = 5$ K) presented in Fig. 9, we also show in Figs. 10 and 11 both low- and high-temperature results for a nonzero detuning of 0.1 meV (the exact parameters are given in the captions).

## APPENDIX I: POLARITON PARAMETERS AND DISCUSSION OF ERRORS

Having shown the behavior of the real polariton frequencies $\omega_{1,2}$ and linewidths $\Gamma_{1,2}$ in Fig. 3 of the main text, we provide for completeness the amplitudes of the biexponential fit Eq. (30) in Fig. 12. This figure addresses both excitonic and photonic polarization, $P_{XX}$ and $P_{CC}$ (black and red, respectively), comparing results from the full calculation in the 15-neighbor approach (symbols) and the analytic approximation Eq. (25) (lines).

Figure 13 shows the error in calculation of the linewidths $\Gamma_{1,2}$ via the Trotter decomposition as function of the coupling strength $g$. This error was estimated as the arithmetic average of the errors for $L = 13$ and 14, treating $L = 15$ as the "exact" solution. We see that the relative error reaches small values of $10^{-5}$ for $g = 50\,\mu$eV and scales as $\propto g^3$ up to $g = 0.5$ meV in agreement with the $g^3$ dependence of the phonon linewidth contribution $\bar{\Gamma}_{\rm ph}$ shown in Eq. (36). Above $\sim$0.5 meV, the error saturates at a level below 1%. While this gives a qualitative picture of the behavior of the error with exciton-cavity coupling strength $g$, one can obtain a more precise estimate of the error by using the exponential dependence on $L$, which is demonstrated for $g = 0.6$ meV in the inset to Fig. 2(b) of the main text. Deviation from the exponential law and a quicker reduction of the error at larger $L$ seen in the inset is a natural consequence of taking the $L = 15$ calculation as exact when evaluating the relative error; if we were to take the true exact solution, we would anticipate a continuation of this exponential trend. One can obviously further refine the estimate of the error by making an extrapolation of all the values of the long-time dependence Eq. (26) to $L \to \infty$, using the observed exponential law.


[1] K. Hennessy, A. Badolato, M. Winger, D. Gerace, M. Atatüre, S. Gulde, S. Fält, E. L. Hu, and A. Imamoğlu, Nature **445**, 896 (2007).

[2] E. T. Jaynes and F. W. Cummings, Proc. IEEE **51**, 89 (1963).

[3] E. del Valle, F. P. Laussy, and C. Tejedor, Phys. Rev. B **79**, 235326 (2009).

[4] J. Kasprzak, S. Reitzenstein, E. A. Muljarov, C. Kistner, C. Schneider, M. Strauss, S. Höfling, A. Forchel, and W. Langbein, Nat. Mater. **9**, 304 (2010).

[5] R. J. Thompson, G. Rempe, and H. J. Kimble, Phys. Rev. Lett. **68**, 1132 (1992).

[6] S. Reitzenstein and A. Forchel, J. Phys. D **43**, 033001 (2010).

[7] Y. Ota, D. Takamiya, R. Ohta, H. Takagi, N. Kumagai, S. Iwamoto, and Y. Arakawa, Appl. Phys. Lett. **112**, 093101 (2018).

[8] I. Wilson-Rae and A. Imamoğlu, Phys. Rev. B **65**, 235311 (2002).

[9] D. P. S. McCutcheon and A. Nazir, New J. Phys. **12**, 113042 (2010).

[10] P. Kaer, T. R. Nielsen, P. Lodahl, A.-P. Jauho, and J. Mork, Phys. Rev. Lett. **104**, 157401 (2010).

[11] Y. Ota, S. Iwamoto, N. Kumagai, and Y. Arakawa, arXiv:0908.0788.

[12] U. Hohenester, Phys. Rev. B **81**, 155303 (2010).

[13] C. Roy and S. Hughes, Phys. Rev. Lett. **106**, 247403 (2011).

[14] M. Glässl, L. Sorgel, A. Vagov, M. D. Croitoru, T. Kuhn, and V. M. Axt, Phys. Rev. B **86**, 035319 (2012).

[15] D. G. Nahri, F. H. A. Mathkoor, and C. H. R. Ooi, J. Phys.: Condens. Matter **29**, 055701 (2016).

[16] A. Nazir and D. P. S. McCutcheon, J. Phys.: Condens. Matter **28**, 103002 (2016).
[17] G. Hornecker, A. Auffèves, and T. Grange, Phys. Rev. B **95**, 035404 (2017).
[18] U. Hohenester, A. Laucht, M. Kaniber, N. Hauke, A. Neumann, A. Mohtashami, M. Seliger, M. Bichler, and J. J. Finley, Phys. Rev. B **80**, 201311(R) (2009).
[19] M. Calic, P. Gallo, M. Felici, K. A. Atlasov, B. Dwir, A. Rudra, G. Biasiol, L. Sorba, G. Tarel, V. Savona, and E. Kapon, Phys. Rev. Lett. **106**, 227402 (2011).
[20] D. Valente, J. Suffczynski, T. Jakubczyk, A. Dousse, A. Lemaitre, I. Sagnes, L. Lanco, P. Voisin, A. Auffeves, and P. Senellart, Phys. Rev. B **89**, 041302(R) (2014).
[21] S. L. Portalupi, G. Hornecker, V. Giesz, T. Grange, A. Lemaître, J. Demory, I. Sagnes, N. D. Lanzillotti-Kimura, L. Lanco, A. Auffèves, and P. Senellart, Nano Lett. **15**, 6290 (2015).
[22] K. Müller, K. A. Fischer, A. Rundquist, C. Dory, K. G. Lagoudakis, T. Sarmiento, Y. A. Kelaita, V. Borish, and J. Vučković, Phys. Rev. X **5**, 031006 (2015).
[23] G. D. Mahan, *Many-Particle Physics* (Springer US, New York, 2000).
[24] B. Krummheuer, V. M. Axt, and T. Kuhn, Phys. Rev. B **65**, 195313 (2002).
[25] E. A. Muljarov and R. Zimmermann, Phys. Rev. Lett. **93**, 237401 (2004).
[26] D. E. Makarov and N. Makri, Chem. Phys. Lett. **221**, 482 (1994).
[27] E. Sim, J. Chem. Phys. **115**, 4450 (2001).
[28] A. Vagov, M. D. Croitoru, V. M. Axt, T. Kuhn, and F. M. Peeters, Phys. Rev. Lett. **98**, 227403 (2007).
[29] A. Vagov, M. Glassl, M. D. Croitoru, V. M. Axt, and T. Kuhn, Phys. Rev. B **90**, 075309 (2014).
[30] M. Cygorek, A. M. Barth, F. Ungar, A. Vagov, and V. M. Axt, Phys. Rev. B **96**, 201201(R) (2017).
[31] A. M. Barth, A. Vagov, and V. M. Axt, Phys. Rev. B **94**, 125439 (2016).
[32] E. A. Muljarov, T. Takagahara, and R. Zimmermann, Phys. Rev. Lett. **95**, 177405 (2005).
[33] Y.-J. Wei, Y. He, Y.-M. He, C.-Y. Lu, J.-W. Pan, C. Schneider, M. Kamp, S. Höfling, D. P. McCutcheon, and A. Nazir, Phys. Rev. Lett. **113**, 097401 (2014).
[34] T. Grange, G. Hornecker, D. Hunger, J.-P. Poizat, J.-M. Gerard, P. Senellart, and A. Auffeves, Phys. Rev. Lett. **114**, 193601 (2015).
[35] J. Iles-Smith, D. P. S. McCutcheon, A. Nazir, and J. Mørk, Nat. Phot. **11**, 521 (2017).
[36] F. Albert, K. Sivalertporn, J. Kasprzak, M. Strauß, C. Schneider, S. Höfling, M. Kamp, A. Forchel, S. Reitzenstein, E. A. Muljarov, and W. Langbein, Nat. Comm. **4**, 1747 (2013).
[37] C. Dory, K. A. Fischer, K. Müller, K. G. Lagoudakis, T. Sarmiento, A. Rundquist, J. L. Zhang, Y. Kelaita, and J. Vučković, Sci. Rep. **6**, 25172 (2016).